1-1-2019

High-degree gravity modes in the single sdB star HD 4539

R. Silvotti

M. Uzundag

A. S. Baran

R. H. Østensen
Missouri State University

J. H. Telting

See next page for additional authors

Recommended Citation

Silvotti, R., M. Uzundag, A. S. Baran, R. H. Østensen, J. H. Telting, U. Heber, M. D. Reed, and M. Vŭcković. "High-degree gravity modes in the single sdB star HD 4539." Monthly Notices of the Royal Astronomical Society 489, no. 4 (2019): 4791-4801.

Monthly Notices
of the
ROYAL ASTRONOMICAL SOCIETY

MNRAS **489,** 1556–1571 (2019)
Advance Access publication 2019 August 12

doi:10.1093/mnras/stz2209

K2 observations of the sdBV + dM/bd binaries PHL 457 and EQ Psc

A. S. Baran [1★] J. H. Telting,[2] C. S. Jeffery [3] R. H. Østensen,[4] J. Vos,[5] M. D. Reed[4] and M. Vŭcković[6]

[1]*Obserwatorium na Suhorze, Uniwersytet Pedagogiczny, ul. Podchorążych 2, 30-084 Kraków, Polska*
[2]*Nordic Optical Telescope, Rambla José Ana Fernández Pérez 7, E-38711 Breña Baja, Spain*
[3]*Armagh Observatory and Planetarium, College Hill, Armagh BT61 9DG, UK*
[4]*Department of Physics, Astronomy, and Materials Science, Missouri State University, Springfield, MO 65897, USA*
[5]*Institut für Physik und Astronomie, Universität Potsdam, Karl-Liebknecht-Str. 24/25, D-14476 Golm, Germany*
[6]*Instituto de Física y Astronomía, Universidad de Valparaiso, Gran Bretaña 1111, Playa Ancha, Valparaíso 2360102, Chile*

Accepted 2019 August 7. Received 2019 August 7; in original form 2019 May 24

ABSTRACT

We present an analysis of two pulsating subdwarf B stars PHL 457 and EQ Psc observed during the *K2* mission. The *K2* light curves of both stars show variation consistent with irradiation of a cooler companion by the hot subdwarf. They also show higher frequency oscillations consistent with pulsation. Using new spectroscopic data, we measured the radial velocity, effective temperature, surface gravity, and helium abundance of both hot subdwarfs as a function of orbital phase. We confirm the previously published spectroscopic orbit of PHL 457, and present the first spectroscopic orbit of EQ Psc. The orbital periods are 0.313 and 0.801 d, respectively. For EQ Psc, we find a strong correlation between $T_{\rm eff}$ and orbital phase, due to contribution of light from the irradiated companion. We calculated amplitude spectra, identified significant pulsation frequencies, and searched for multiplets and asymptotic period spacings. By means of multiplets and period spacing, we identified the degrees of several pulsation modes in each star. The g-mode multiplets indicate subsynchronous core rotation with periods of 4.6 d (PHL 457) and 9.4 d (EQ Psc). We made spectral energy disctribution (SED) fits of PHL 457 and EQ Psc using available broad-band photometry and *Gaia* data. While the SED of PHL 457 shows no evidence of a cool companion, the SED for EQ Psc clearly shows an infrared (IR) access consistent with a secondary with a temperature of about 6800 K and a radius of 0.23 $R_{\odot}$. This is the first detection of an IR access in any sdB + dM binary.

Key words: binaries: general – stars: individual (PHL 457, EQ Psc) – stars: oscillations (including pulsations).

1 INTRODUCTION

Subdwarf B (sdB) stars are hot compact stars located on the blue extension of the horizontal branch (HB). The progenitors of sdB stars on the main sequence are around one solar mass, and must have lost significant mass to leave only a tiny fraction of their hydrogen envelopes. The envelope loss must happen before helium ignition, otherwise it will become just a normal HB star. Following helium ignition the star evolves to an equilibrium configuration with a surface effective temperature ($T_{\rm eff}$) between 20 000 and 40 000 K, the logarithm of surface gravity ($\log g$ / cm s^{-2}) between 5 and 6, and a surface helium abundance strongly depleted compared to solar. The surface distribution of elements heavier than helium differs significantly from star to star (Geier 2013).

Stellar oscillations in sdB stars were first detected by Kilkenny et al. (1997). Models which predict unstable pulsation modes in sdBs were first published by Charpinet et al. (1997). To date, the sample of pulsating sdB stars is approaching a hundred, with half of the sample discovered with the space photometry missions *Kepler* and *K2*.

This paper continues our work on pulsating sdB stars (hereafter: pulsating sdB or sdBV stars) using photometric data collected during the *K2* mission of the *Kepler* spacecraft. With an emphasis on finding new sdBV stars, monitoring known sdBVs and identifying their pulsation modes, we have collected data on 31 sdBVs, with eight already published: Jeffery & Ramsay (2014), Reed et al. (2016), Bachulski et al. (2016), Baran et al. (2017), Ketzer et al. (2017), and Reed et al. (2018b). These papers

★ E-mail: andysbaran@gmail.com

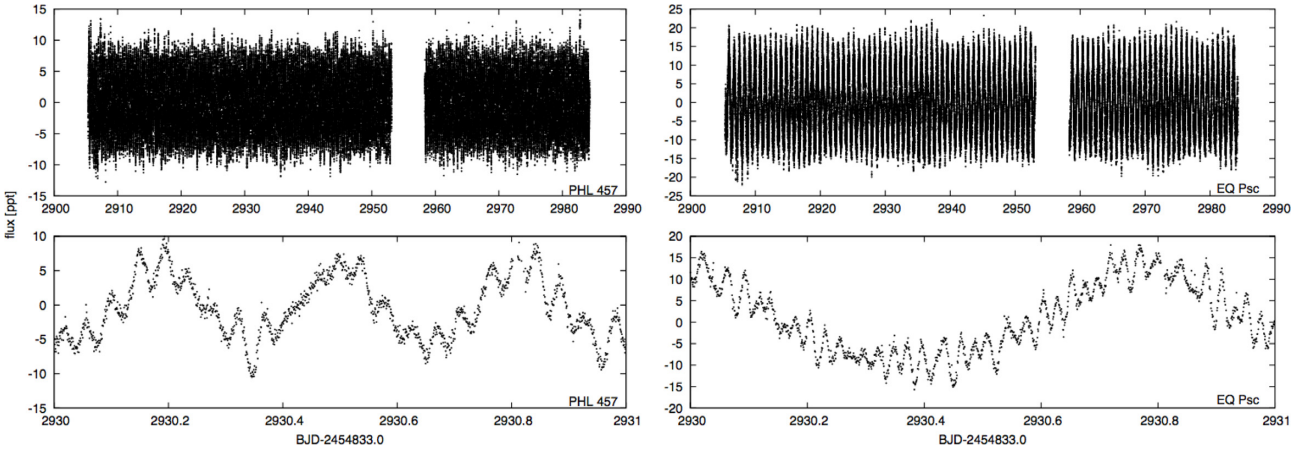

Figure 1. Light curves of PHL 457 (left) and EQ Psc (right) obtained during Campaign 12 of *K2*. Top panels show the entire processed, truster-firings removed, data sets, while the bottom panels show close-ups of the flux variations.

Table 1. The ALFOSC RV data of PHL 457. RV and errors are given in km s^{-1}, and t_{exp} in seconds.

BJD	RV	Error	S/N	t_{exp}
2458304.7043687	12.5	5.1	138.0	300
2458307.6741738	30.6	5.4	176.4	300
2458317.7406818	29.3	5.3	132.8	300
2458338.6255085	21.3	6.1	120.3	300
2458349.7416172	18.8	4.6	120.0	300
2458356.5959250	32.6	6.6	138.0	300
2458379.6784356	27.4	5.3	100.1	300
2458380.5947331	40.5	6.7	176.1	300
2458391.6630396	11.7	4.9	127.5	300
2458393.5229922	23.2	4.4	146.7	300
2458429.5285782	11.3	3.2	126.4	300
2458453.4487755	20.2	3.5	126.8	300

revealed interesting and important features of pulsation in sdBVs, including rotational multiplets and asymptotic period spacings. Our primary goal is to identify the non-radial pulsation modes associated with each pulsation frequency. Each non-radial mode can be represented as a 3D spherical harmonic characterized by three integers describing the number of nodes in radial, longitudinal, and latitudinal directions. Mode geometry has been widely described (e.g. Handler 2013). Such an identification is the first step in applying asteroseismology to study stellar interiors.

The maximum duration of *K2* observations for any star (80 d) is much less than the maximum for the main *Kepler* mission (four years), though the temporal window is still better than for any sdBV observed from the ground. A typical *K2* observation gives a frequency resolution of 0.2 μHz. The average noise level in amplitude spectra depends on time coverage but also on a star's brightness, and for the brightest ($K_p = 10.4$) and faintest ($K_p = 18.1$) sdBV observed during *K2,* it is 1.3 and 180 parts per million (ppm), respectively.

Asteroseismic analyses of *Kepler*-observed sdBV stars have revealed interesting and useful features. Frequency multiplets and g-mode asymptotic period sequences have been used to identify modes. Most are of low degree ($\ell \leq 2$) although some of higher degree ($3 \leq \ell \leq 8$) have been detected, usually in the 'intermediate region' of 400–700 μHz (Telting et al. 2014; Foster et al. 2015). Detected g-mode period spacings range from 207 (Reed et al. 2019;

Table 2. The RV data of EQ Psc. The MagE velocities have been shifted by + 23.68 km s^{-1} to match those of ALFOSC (see Section 3.2). RV and errors are given in km s^{-1}, and t_{exp} in seconds.

BJD	RV	Error	S/N	t_{exp}	
2457564.71245	38.9	5.0	115.8	600	ALFOSC
2457590.59335	−1.8	5.0	111.7	400	ALFOSC
2457590.71830	−0.0	5.3	115.4	300	ALFOSC
2457591.62294	30.5	8.1	92.4	300	ALFOSC
2457591.71701	57.3	7.1	90.4	300	ALFOSC
2457622.58715	−8.8	5.0	136.2	300	ALFOSC
2457622.69687	4.6	5.0	108.3	300	ALFOSC
2457629.53755	56.3	5.0	108.6	360	ALFOSC
2457629.70480	16	12	72.0	300	ALFOSC
2457636.75262	45.4	5.0	97.8	300	ALFOSC
2457652.66821	58.9	5.0	92.7	300	ALFOSC
2457656.61199	54.5	7.5	86.5	300	ALFOSC
2457672.53221	40.3	5.0	117.5	300	ALFOSC
2457679.56873	−13.3	5.9	109.3	300	ALFOSC
2457680.58848	50.4	5.0	110.2	300	ALFOSC
2457681.55218	53.4	5.0	117.5	300	ALFOSC
2457681.65579	33.3	6.9	103.7	300	ALFOSC
2457721.38922	41.6	5.2	110.7	300	ALFOSC
2457729.31964	11.1	5.0	132.3	300	ALFOSC
2457729.45902	60.5	7.5	79.1	420	ALFOSC
2457730.39489	59.1	5.0	133.0	300	ALFOSC
2457739.31712	31.2	8.9	81.7	300	ALFOSC
2457758.31594	66.5	8.1	68.2	300	ALFOSC
2457778.33348	77.8	8.7	67.0	300	ALFOSC
2458014.66752	63.6	3.9	135.0	300	MagE
2458014.67125	60.3	3.5	128.1	300	MagE
2458014.67499	63.3	4.9	128.7	300	MagE
2458014.70654	57.8	5.5	136.2	300	MagE
2458014.71028	59.2	3.3	132.1	300	MagE
2458014.71402	64.7	5.6	124.8	300	MagE
2458014.76844	47.0	5.4	114.2	300	MagE
2458014.77217	50.2	6.4	111.4	300	MagE
2458014.77591	47.9	5.3	120.0	300	MagE
2458014.81598	30.8	5.4	115.5	400	MagE
2458014.82088	36.6	4.5	119.5	400	MagE
2458014.82577	35.6	5.4	117.2	400	MagE
2458014.86498	27.9	6.2	80.1	300	MagE
2458014.86872	23.8	5.1	79.8	300	MagE
2458014.87252	22.3	6.5	78.9	300	MagE

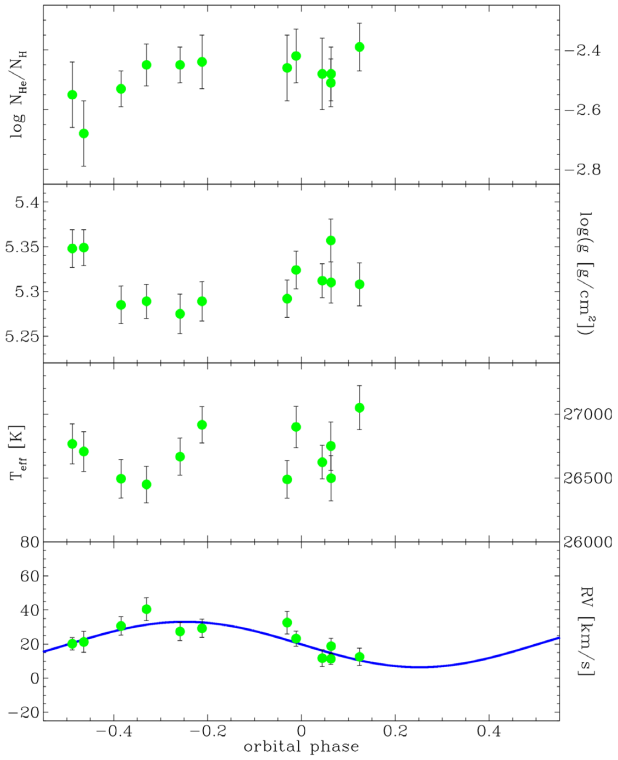

Figure 2. Results of LTE model fits for the sdB in PHL 457. The bottom panel shows the RV values.

Table 3. Results of a circular orbital fit after folding the RVs of PHL 457 to orbital phase.

γ	System velocity (km s^{-1})	19.7(1.5)
K_1	Radial velocity (km s^{-1})	13.3(3.1)
	Rms (km s^{-1})	7.03

Table 4. The results of the SED fit for PHL 457, based on a *Gaia* distance of 577 ± 21 pc and extinction $E(B-V) = 0.023^{+0.016}_{-0.023}$. In the first fit, $T_{\rm eff}$ is allowed to vary. In the second fit, it is fixed to the spectroscopic value. The mass is determined from the radius of the SED fit and the surface gravity of the spectroscopic fit.

Fit	$T_{\rm eff}$ (K)	R ($R_\odot$)	L ($L_\odot$)	M ($M_\odot$)	Red. χ^2
Free	26940 ± 750	0.23 ± 0.01	22.8 ± 2.3	0.39 ± 0.05	2.75
Fixed	26670 ± 60	0.23 ± 0.01	22.5 ± 1.6	0.39 ± 0.05	2.88

Baran et al. 2012) to 273 s (Østensen et al. 2012) with most near 250 s (Reed et al. 2018a). Asymptotic sequences often show a 'hook' structure (e.g. Baran & Winans 2012) and occasionally include trapped modes (e.g. Østensen et al. 2014; Uzundag et al. 2017) which have been related to core overshooting (e.g. Guo & Li 2018). While not asymptotic, models predict p-mode overtones spaced in frequency by 800–1100 μHz (Charpinet et al. 2002). Observations have yielded a mixture of results with three sdBV stars in agreement (Baran et al. 2009; Foster et al. 2015; Reed et al. 2019) and two with much smaller spacings (Baran et al. 2012; Reed et al. 2019).

Frequency multiplets allow rotation periods of sdBV stars to be determined, with typical seismic rotation periods of tens of days. This includes short-period binaries with orbital periods down to

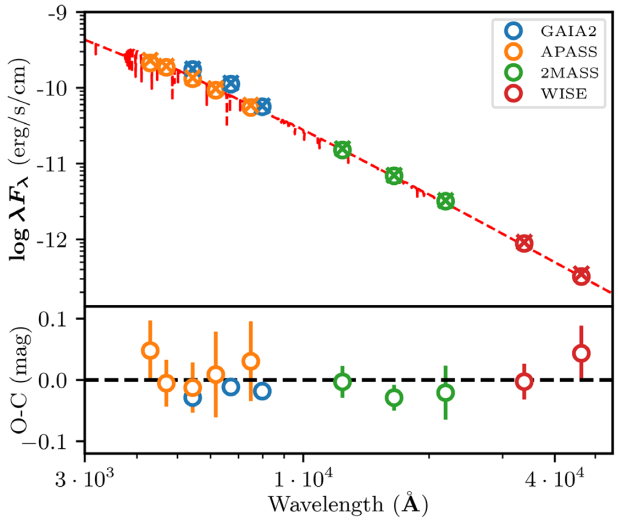

Figure 3. The SED of PHL 457 together with the best-fitting model. The observed fluxes are shown as open circles, while the calculated fluxes are shown as crosses. The best-fitting TMAP model is shown as a red dashed line.

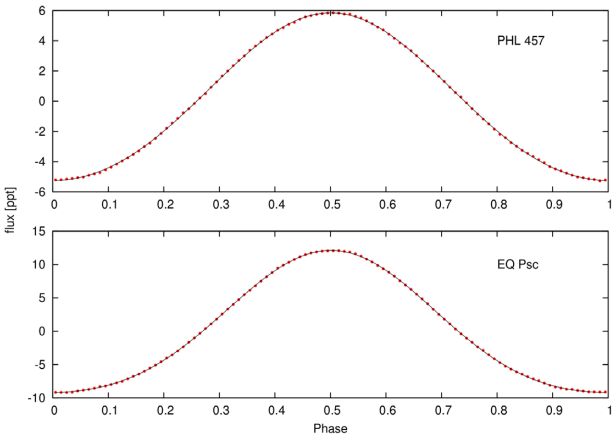

Figure 4. Light curves of PHL 457 and EQ Psc phased and binned over their orbital periods.

0.5 d (e.g. Telting et al. 2012; Baran et al. 2016), indicating that the sdBV components of these post-common-envelope binaries rotate subsynchronously. For hybrid pulsators, it is occasionally possible to determine simultaneously rotation periods for the envelope (from p modes) and the deeper interior (from g modes). Results so far indicate three uniform rotators (Baran et al. 2012; Kern et al. 2018; Reed et al. 2019) and three differential rotators (Baran et al. 2017; Foster et al. 2015; Reed et al. 2019) with envelopes rotating more rapidly than interiors.

In this paper, we present our analysis of two especially interesting sdB stars observed during the *K2* mission. PHL 457 and EQ Psc have low-mass companions and their light curves show orbital flux variation indicating orbital periods of 0.3 and 0.8 d, respectively. In addition, both stars are rich hybrid pulsators. We use seismic tools including frequency multiplets and asymptotic period spacings to identify pulsation modes. These data allow us to search for evidence of differential rotation and p- and g-mode overtone spacings. We present new spectroscopic data of both targets to constrain effective temperature, surface gravity, and helium abundance and to derive

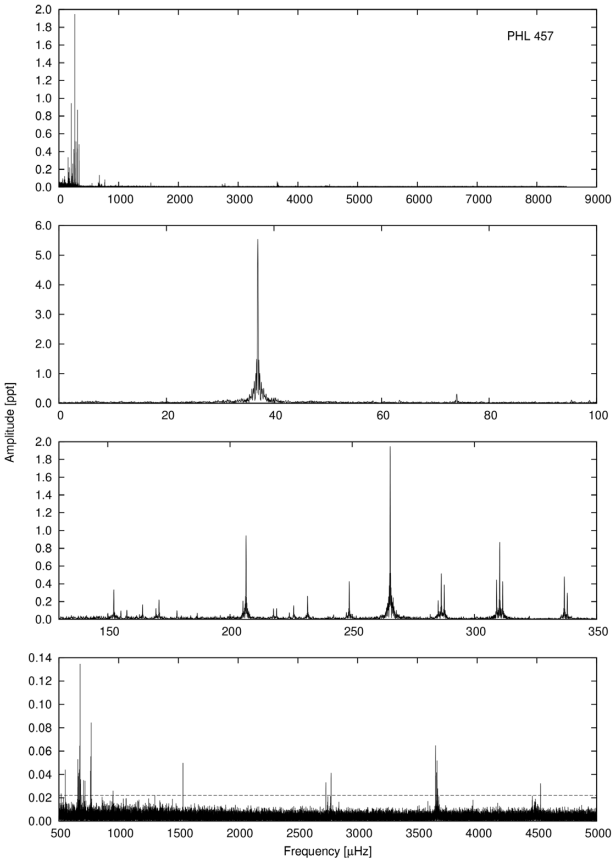

Figure 5. Amplitude spectrum of PHL 457 up to the Nyquist frequency (8496 μHz) showing both g- and p-mode regions. The binary frequency and its first harmonic are removed from the top panel and are shown in the second panel from top. Close-ups of the g- and p-mode regions are shown in the two lower panels. The dashed line in the bottom panel represents the 5σ confidence threshold.

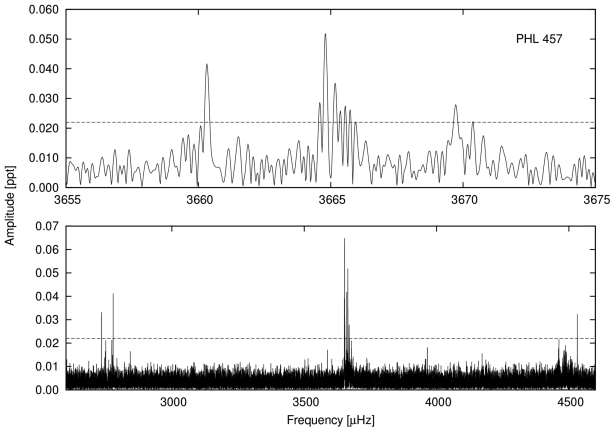

Figure 6. A close-up of the p-mode region of PHL 457. The top panel shows a possible multiplet while the bottom panel shows possible frequency grouping, indicative of a consecutive radial order of modes as the frequency increases. The dashed line represents the 5σ confidence threshold.

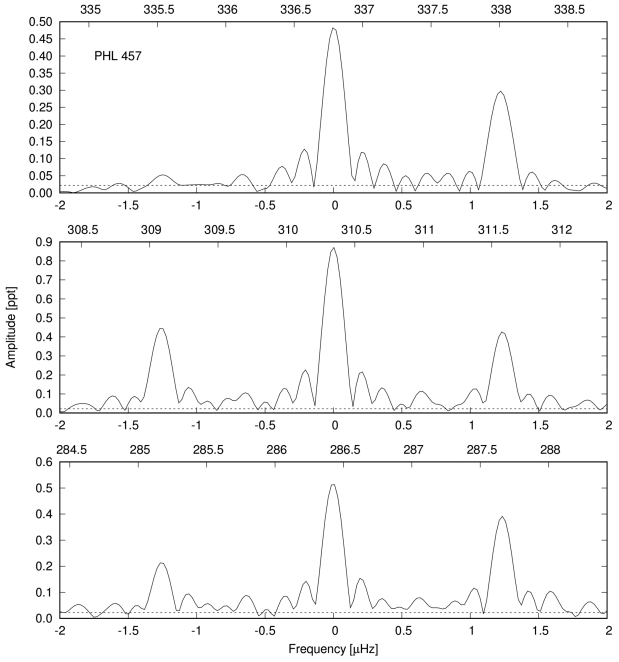

Figure 7. Three examples of the multiplets we found in the amplitude spectrum of PHL 457. Top horizontal axes show actual frequencies in μHz, while bottom axes show relative scale from central components. The dashed line represents the 5σ confidence threshold.

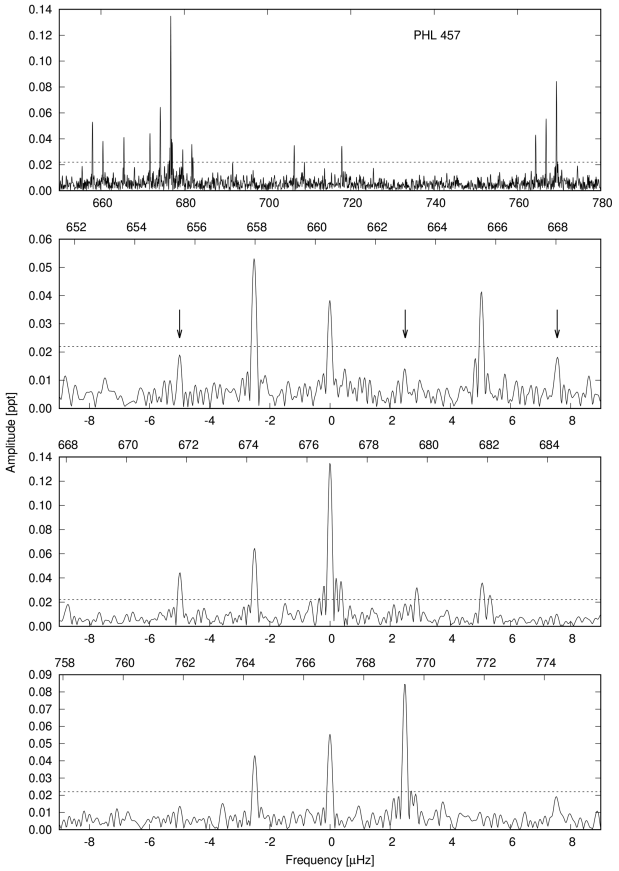

Figure 8. A close-up of the intermediate region in PHL 457. The top panel shows the entire region, while the lower panels show multiplet candidates. The splitting is consistent with the one for high radial order g or p modes, if estimated from triplets plotted in Fig. 7. The dashed line represents the 5σ confidence threshold.

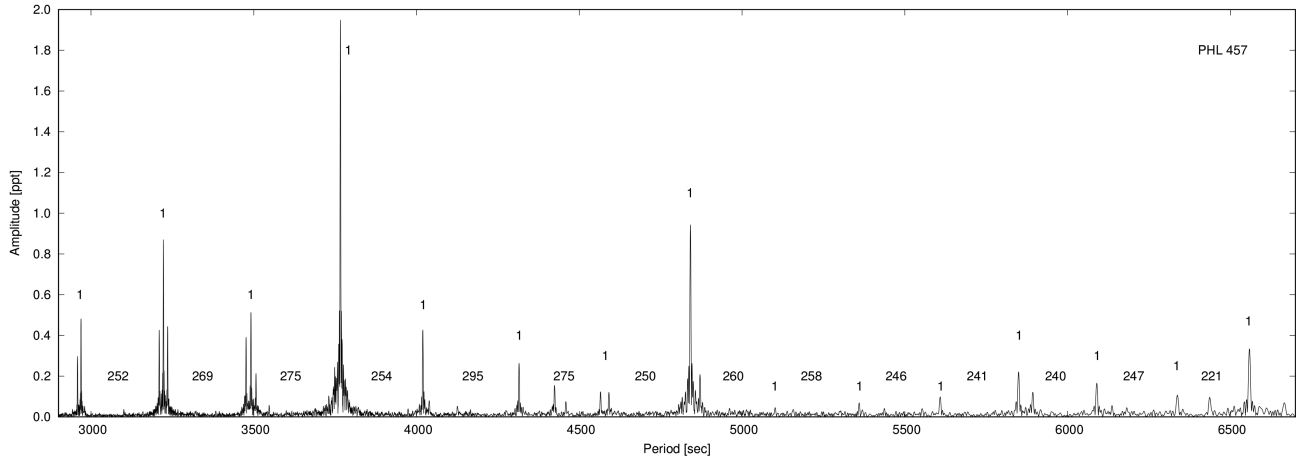

Figure 9. The amplitude spectrum of PHL 457 as a function of period. Numbers denote the modal degree (ℓ) of identified modes and the spacing between them.

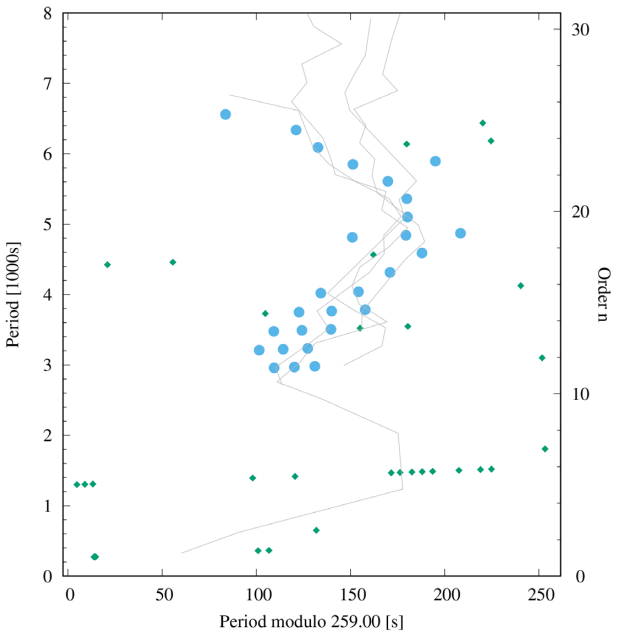

Figure 10. Échelle diagram for dipole modes detected in PHL 457. Blue circles denote dipole modes, while green squares denote unidentified frequencies. Black transparent lines represent échelle diagrams of four other sdBVs, KIC 10553698 (Østensen et al. 2014), KIC 1179657 (Baran & Winans 2012), KIC 8302197 (Baran et al. 2015b), and KIC 2697388 (Baran 2012).

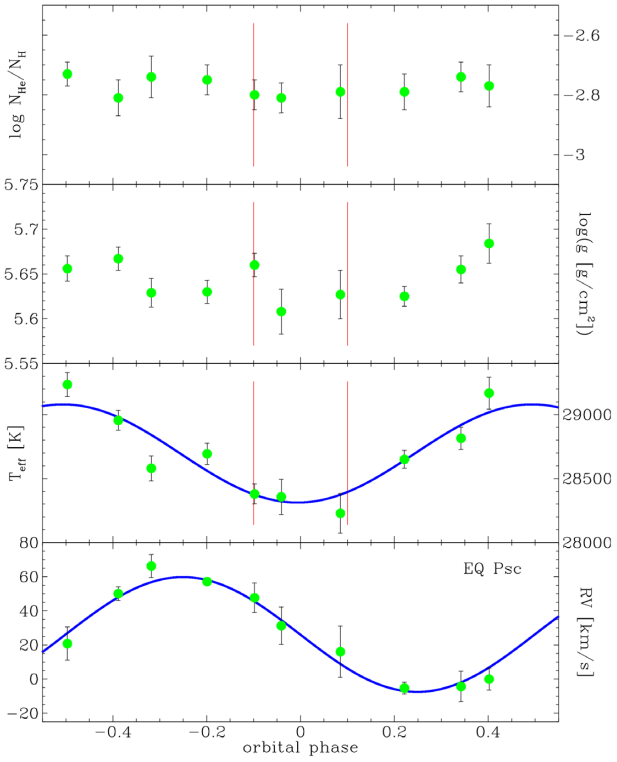

Figure 11. Results of LTE model fits for spectra binned to orbital phase. The bottom panel shows the binned RV values. The second panel from bottom shows a sinusoidal fitted to the measurements of the temperature of the subdwarf in EQ Psc. The latter are affected by additional flux from the illuminated side of the secondary (see Fig. 4). The unilluminated side of the secondary is seen around orbital phase 0.0 (red delimeters). The secondary's contribution to the total flux is therefore at a minimum so that this phase most accurately provides the sdB atmosphere parameters. The two upper panels show the variation in surface gravity and He abundance which does not show any significant phase dependence.

spectroscopic orbits for both targets. In order to calculate and fit the spectral energy disctribution (SED) we have used absolute photometric measurements obtained from the *Gaia* DR2 catalogue (Evans et al. 2018; Riello et al. 2018), the APASS (AAVSO Photometric All Sky Survey) DR9 catalogue (Henden et al. 2016), 2MASS (Two Micron All Sky Survey, Skrutskie et al. 2006), and *WISE* (*Wide-field Infrared Survey Explorer*, Cutri & et al. 2012). Even though *GALEX* DR 5 data (Bianchi et al. 2011) are available for both systems, we have not used it as the errors on the fluxes are too high (see e.g. Camarota & Holberg 2014).

2 K2 DATA

PHL 457 and EQ Psc were observed by the *Kepler* spacecraft during the *K2* phase of its mission. The observations of both stars were taken in Campaign 12, which started on 2016 December 15 and

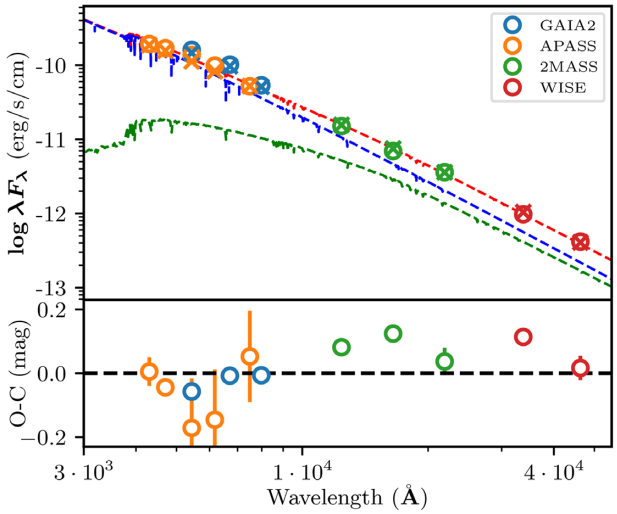

Figure 12. The SED of EQ Psc together with the best-fitting model. The observed fluxes are shown as open circles while the calculated fluxes are shown as crosses. The best-fitting two-star model is shown as a red dashed line with the cool and hot component shown respectively by green and blue lines, respectively.

finished on 2017 March 4. We downloaded all available data from the 'Barbara A. Mikulski Archive for Space Telescopes'.[1] We used the short-cadence (SC) data, sampled at almost 1 min time resolution, since they allow us to reasonably sample the orbital flux variation, and to sample an amplitude spectrum beyond the g-mode region, which means that both g- and p-mode regions are covered.

First, we used standard IRAF tasks to extract fluxes from the pixel tables. Next, we used our custom PYTHON scripts to de-correlate fluxes in *X*- and *Y*-directions around a 2D pixel mask on each target. This latter step removed the flux dependence on position on the CCD and the resultant light curve was free of the signatures of thruster firings. Finally, we represent the light variations as residual flux ($a = f/\bar{f} - 1$) in *parts per thousand* (ppt). We show the final light curves of both stars in Fig. 1.

3 SPECTROSCOPIC DATA

3.1 ALFOSC@NOT

Low-resolution ($R = 2000$) spectra have been collected using the 2.56 m Nordic Optical Telescope with Alhambra Faint Object Spectrograph and Camera (ALFOSC), grism number 18 and a 0.5 arcsec slit. The resulting resolution is 2.2 Å. We secured 12 spectra of PHL 457 (2018 June 5–November 30) and 24 of EQ Psc (2016 June 25–2017 January 24) using this setup. For PHL 457, exposure times were 300 s, yielding S/N ≈100–176. For EQ Psc, exposure times ranged from 300 to 600 s with S/N ≈67–136.

These data were all reduced and analysed identically. Standard reduction steps within IRAF include bias subtraction, removal of pixel-to-pixel sensitivity variations, optimal spectral extraction, and wavelength calibration based on helium arc-lamp spectra. The target spectra and the mid-exposure times were shifted to the barycentric frame of the Solar system. The spectra were normalized to place the continuum at unity by comparing with a model spectrum for stars with similar physical parameters as we find for the targets.

[1] archive.stsci.edu

Radial velocities (RVs) were derived with the FXCOR package in IRAF. We used the Hβ, Hγ, Hδ, Hζ, and Hη lines to determine the RVs, and used a spectral model fit as an RV template. Observing logs and measured RVs are given in Tables 1 and 2.

3.2 MagE@Magellan

We collected 15 additional spectra of EQ Psc using The Magellan Echellette (MagE, Marshall et al. 2008) spectrograph at the Magellan Telescope. These spectra were obtained on the night of 2017 September 18 with a 1.0 arcsec slit yielding a resolution of $R = 4100$. See Table 2 for the observing log.

The spectra were reduced with the CarPi PYTHON package for spectroscopic data reduction (Kelson et al. 2000; Kelson 2003). The MagE spectrograph has a spectral range of 3000–10 000 Å, but the CarPi reduction pipeline only reduces the wavelength range 3500–7000 Å. ThAr spectra were obtained every 3–4 science spectra, and furthermore we have used interstellar absorption lines of Na and Ca to further increase the wavelength stability. RVs of all spectra were obtained by cross-correlating with a template spectrum using the Hα, Hβ, Hγ, Hδ, Hζ, Hη, and He I line at 5875 Å. RV errors were determined using a Monte Carlo simulation with 100 iterations. A more detailed description of the RV determination can be found in Vos et al. (2019).

Since the MagE data cover only a quarter of the orbit, they are insufficient to improve the orbital solution on their own. We also found it necessary to offset the MagE RV values by $+23.68$ km s^{-1} to make them consistent with the extrapolated ALFOSC RV curve (see Section 5.1). The origin of this systematic shift is not known.

4 PHL 457

PHL 457: $\alpha_{2000} = 23^{\rm h}19^{\rm m}24.44^{\rm s}$, $\delta_{2000} = -08^\circ 52' 37.9''$. Edelmann et al. (2005) described the first attempt to measure the orbital period of this system. Too few RV points resulted in a constraint of <3 d. Blanchette et al. (2008) reported $T_{\rm eff}$ to be 28.2 or 29.3 kK and $\log g/{\rm cm\,s^{-2}}$ of 5.5 or 5.6, from NLTE and LTE[2] analyses, respectively. They also discussed the abundances of specific elements derived from far-ultraviolet (FUV)-spectra obtained with the *FUSE* satellite and identified the star as a long-period pulsator of the V1093 Her type. The orbital period remained unconstrained. Geier & Heber (2012) estimated $T_{\rm eff} = 26\,500$ K, and found that the rotation of the sdB star is not synchronized with its orbital motion. They measured $K_1 = 13.0(2)$ km s^{-1}, and derived the first ephemeris with an orbital period around 0.313 d. Schaffenroth et al. (2014) presented the first spectroscopically solved orbit, and found the mass of the companion to be at least 0.027 $M_\odot$, indicating a brown dwarf. Kilkenny & Koen (2016) interpreted a flux variation as two pulsation modes and likely a reflection effect with a period of 0.31 d. PHL 457 has been monitored with the *Gaia* satellite. The parallax was measured as 1.73(6) mas, which translates to the distance of 577(21) pc. The *Gaia G*-band magnitude was estimated to be nearly 12.94 (Gaia Collaboration 2018).

4.1 Spectroscopic results

After folding the timings of the spectra to orbital phase, using the period found from the *K2* data (Section 4.3), we fitted a

[2] Non-local and local thermodynamic equilibrium.

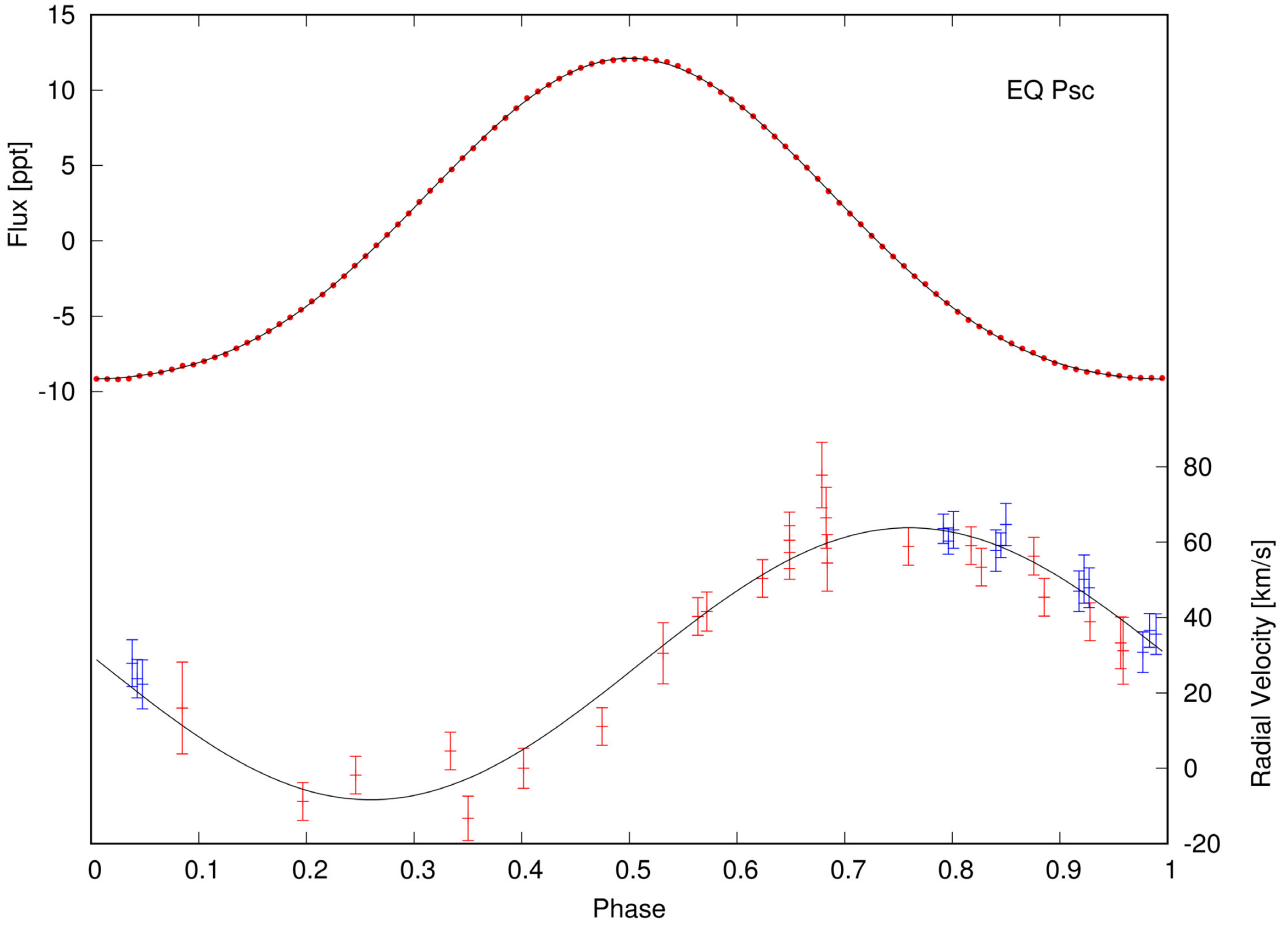

Figure 13. Photometric (upper plot) and RV (lower plot) phased data overlapped with fits. Red symbols in the bottom plot respresent NOT data, while blue symbols represent MagE data.

circular orbit to the RVs from Table 1. We find an RV amplitude of $K_1 = 13.3(3.1)\,\mathrm{km\,s^{-1}}$ (Table 3), and a system velocity of 19.7(1.5) $\mathrm{km\,s^{-1}}$, which are both consistent with the results presented by Schaffenroth et al. (2014). Those authors already argued that the value of K_1 in the mass function implies a lower limit to the companion mass of $M_2 > 0.027\,\mathrm{M_\odot}$, hence a brown dwarf with $28\,\mathrm{M_{Jup}}$, when assuming a canonical mass of the sdB star of $M_1 = 0.47\,\mathrm{M_\odot}$ (Fontaine et al. 2012). Only for inclinations of the orbit smaller than $i < 20^\circ$ the secondary is stellar ($M_2 > 0.08\,\mathrm{M_\odot}$). The distance between the centre of masses of the stars is $1.54 - 1.90\,\mathrm{R_\odot}$ for inclinations $90^\circ > i > 5^\circ$.

We fitted LTE model atmospheres (Heber, Reid & Werner 2000; Edelmann et al. 2003) to the individual spectra to obtain $T_{\rm eff}$, $\log g$, and surface helium-to-hydrogen ratio ($N_{\rm He}/N_{\rm H}$), shown as a function of orbital phase in Fig. 2. Even though the spectra do not sample all orbital phases, it is clear that $T_{\rm eff}$, $\log g$, and $\log(N_{\rm He}/N_{\rm H})$ vary neither significantly nor systematically over the orbit. This is in contrast to the measurements of $T_{\rm eff}$ of EQ Psc discussed in the next section. Taking the average of the fits to all 12 ALFOSC spectra, we find that for the sdB star in PHL 457: $T_{\rm eff} = 26\,690(60)$K, $\log g/\mathrm{cm\,s^{-2}} = 5.312(8)$, and $\log(N_{\rm He}/N_{\rm H}) = -2.487(22)$. Note that the errors quoted here are only chi-squared fitting errors between the observed spectra and the H/He models. Systematic effects from the composition and other model assumptions are not included, and can be on the order of 2000 K in $T_{\rm eff}$ and 0.1 in $\log g/\mathrm{cm\,s^{-2}}$.

4.2 SED and mass determination

The SED obtained from absolute photometry can be used to check the atmospheric parameters obtained from spectroscopy. The photometric measurements used are averages of many taken over an extended period of time and thus regarded as orbital averages. We fit stellar atmosphere models computed with Tübingen NLTE Model-Atmosphere Package (TMAP, Werner et al. 2003) to the observed SEDs. The surface gravity cannot be derived from the SED and is kept fixed at the spectroscopic value. The reddening is obtained from the Stilism dust map (Lallement et al. 2019) as $E(B-V) = 0.023^{+0.016}_{-0.032}$. The distance is obtained by inverting the *Gaia* DR2 parallax. To propagate the errors on the $T_{\rm eff}$, $\log g$, $E(B-V)$, and the distance, these parameters are not kept fixed at the chosen values, but are instead included in the χ^2 determination. A detailed description of the SED fitting procedure can be found in Vos et al. (2013, 2017, 2018). Two fits were performed, such that in the first one $T_{\rm eff}$ was allowed to vary freely, while in the second one, $T_{\rm eff}$ was fixed at the spectroscopic value. The results are given in Table 4. The SED of PHL 457 with free $T_{\rm eff}$ is shown in Fig. 3. The reduced χ^2 values are larger than 1, indicating that the errors on the photometry are likely underestimated. This is a known issue with many photometric catalogues.

There is no significant difference between the fit where $T_{\rm eff}$ is free and fixed to the spectroscopic value. There is also no evidence of the cool companion in the SED. A two-component fit was attempted

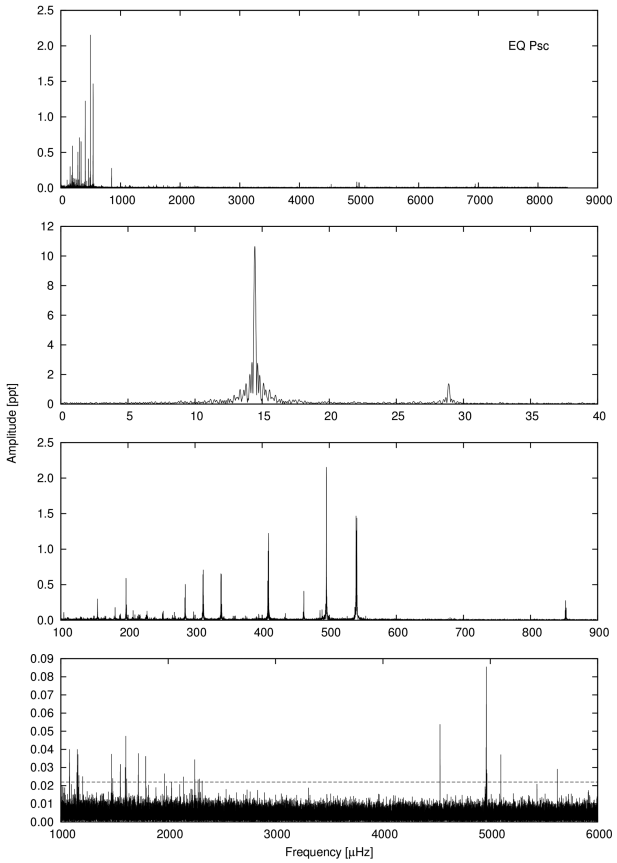

Figure 14. Amplitude spectrum of EQ Psc up to the Nyquist frequency (8496 μHz) showing both g- and p-mode regions. The binary frequency and its first harmonic is removed from top panel and are shown in the second panel from top. Close-ups of the g- and p-mode regions are shown in the bottom two panels. The dashed line in the bottom panel represents the 5σ confidence threshold.

where a blackbody was used to model the contribution of the companion, but the fit could not be improved significantly, with the best χ^2 for a binary fit being 2.63.

Based on the radius from the SED fit and the surface gravity from the spectroscopic fit, we determine the mass of the sdB component in PHL457 as $M = 0.39 \pm 0.05\,\mathrm{M}_{\odot}$. This value is slightly lower than the canonical sdB mass, but is still consistent with an sdB igniting He under degenerate conditions.

4.3 Binary orbit from *K2* data

PHL 457 is a binary system consisting of an sdB star and a cool low-mass companion. After phase folding on the orbital period, the binned light curve is shown in the top panel of Fig. 4. We folded in on the ephemeris

$$T = 2457738.31313(8)\,\mathrm{BJD} + 0.3128907(11)E$$

derived from a sinusoidal fit to the data after removal of other variability (Section 4.4). We chose the reference epoch to be when the sdB star is first at its farthest point from us after commencement of the *K2* observations. The folded light curve has a bell shape (Fig. 4) which is characteristic for binaries where a hot component irradiates a cool companion. It is common that models are used to infer the physical properties of both components of a binary system from a photometric light curve. The result is more reliable when an

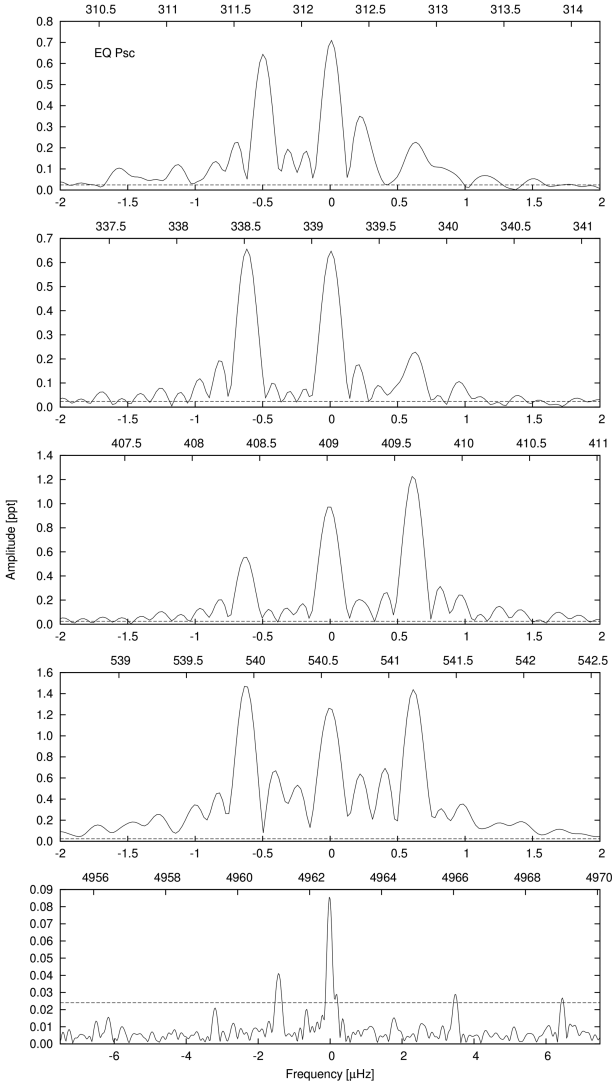

Figure 15. The four upper panels show examples of clear multiplets in the amplitude spectrum of EQ Psc. The bottom panel shows a close-up of the p-mode region with just one possible multiplet candidate. Top horizontal axes show actual frequencies, while bottom axes show relative spacing from central components. The dashed line represents the 5σ confidence threshold.

RV curve is also employed, the light curve is available for multiple filters and shows eclipses. The latter is crucial to avoid degeneracies of solutions. Since we posses neither multicolour photometry nor precise RV follow-up and since the light curve does not show clear eclipses, we simply fit the out-of-eclipse variation. In the absence of eclipses, the shape of the light curve can be modelled by a sum of two cosines phased in such a way that their maxima align, and their minima do not (Østensen et al. 2013). Thus, we fit the light curve with the following function:

$$a/(\mathrm{ppt}) = 5.550(5)\cos(2\pi(\phi + 0.5)) + 0.307(5)\cos(4\pi(\phi + 0.5)) - 0.007(4),$$

where ϕ is orbital phase.

We found no signatures of eclipses down to 0.06 ppt (1 per cent of flux's amplitude). Together with the constraint on R_1 from the SED fit, and while assuming $R_2 \sim 0.09\,\mathrm{R}_{\odot}$ for a brown dwarf, we find an upper limit for the orbital inclination of $i < 78^{\circ}$, from the fact that we do not see eclipses.

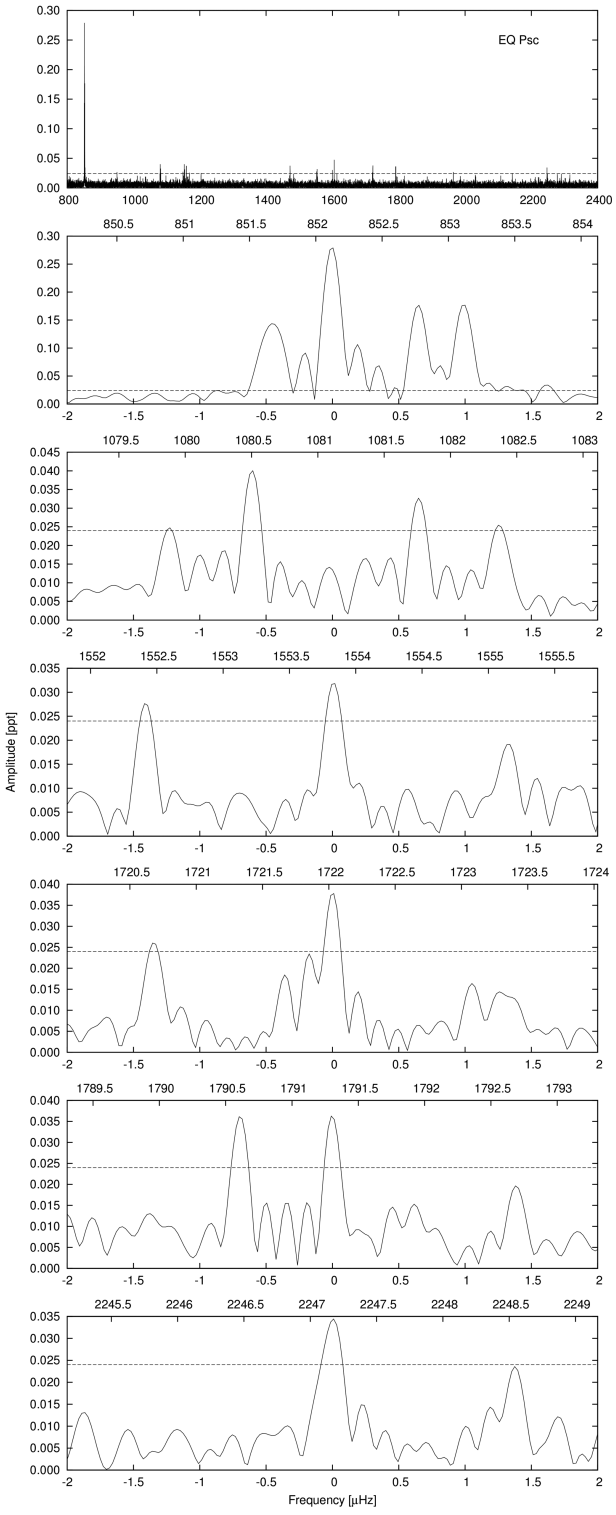

Figure 16. A close-up of the intermediate region in EQ Psc. The top panel shows the entire region, while the lower panels show multiplet candidates. The dashed line represents the 5σ confidence threshold.

4.4 Pulsation properties

We calculated the Fourier transforms from the *K2* data and show the amplitude spectrum in Fig. 5. The top panel contains the entire spectrum up to the Nyquist frequency with the orbital effect removed. The second panel from the top shows the binary frequency with its first harmonic. The third panel from the top shows the frequency range with significant signal in the g-mode region, while the bottom panel shows a wide range of the p-mode region as well as some signal between the g- and p-mode regions. Our analysis confirms Kilkenny & Koen's (2016) report of flux variation likely caused by stellar oscillations.

We used pre-whitening iterations to identify frequencies with amplitudes higher than the detection threshold of 0.022 ppt (Table 5). Following the analysis by Baran, Koen & Pokrzywka (2015a), we defined the detection threshold to be five times the average noise level calculated in the residual amplitude spectrum. We recovered 58 frequencies; most of them located in the g-mode region, and only five in the p-mode region. Two additional frequencies corresponding to the binary orbital frequency and its first harmonic are included ($f_{\rm bin}$, $f_{\rm har}$) in the table. There is also an amplitude bump around 4456 μHz, but the individual amplitudes are below the threshold and therefore not included in the analysis.

The analyses of other sdBV stars observed with the *Kepler* spacecraft, showed that g modes can show asymptotic period spacings, rotationally split multiplets and trapped modes, while p modes may only show rotationally split multiplets. In addition, Baran et al. (2009) reported regions of p modes separated by a few hundreds of μHz, an indication of modes of the same modal degree but differing in radial order (Charpinet et al. 2000). In PHL 457, even though the number of detected p modes is very low, we identified one possible multiplet (at 3665 μHz) and three distinct groups of frequencies indicating a possible sequence in radial order. We show these features in Fig. 6. The frequency splitting in the multiplet is around 4.63 μHz. This multiplet could either be a triplet or a quintuplet with missing components. Higher modal degrees cannot be ruled out. Since the Ledoux constant is close to zero for p modes, a rough estimate of the spin period is 2.5 d, if our interpretation of the multiplet is correct. In contrast, for the rotation of the envelope to be tidally locked to the orbital period, the splitting would be 37 μHz, and not necessarily symmetric around the central component. The bottom panel of Fig. 6 shows three main p-mode groups centred around frequencies of 2734, 3600, and 4500 μHz. The separations between these groups are 920 and 810 μHz, significantly lower than the mean value for p modes of 1.4 mHz. However, the spacings and, more significantly, the corresponding period ratios are very close to those expected for fundamental, first- and second-overtone radial modes (Baran, Pigulski & O'Toole 2008). Such a feature has been previously detected by (Baran et al. 2009) and is roughly consistent with model calculations reported by Charpinet et al. (2002).

The low-frequency region contains 53 frequencies, including 15 frequencies in the so-called intermediate region between 500 and 2000 μHz. We searched for multiplets and equally spaced periods. These two features allow us to estimate the spin period and constrain modal geometry. A common spin period of sdBV stars is around 40 d, which is not easily resolved with *K2* data. Fig. 7 shows some g-mode multiplets. Several PHL 457 frequencies are equally split with a consistent separation of 1.25 μHz. Assuming they are all dipole modes and that the Ledoux constant $C_{\rm nl} = 0.5$ for $\ell = 1$ modes (Charpinet et al. 2000), this splitting translates to a spin period of ≈4.6 d. If we compare this to the binary period (0.31 d), we conclude that PHL 457 is another sdBV star with subsynchronous rotation (e.g. Baran et al. 2016; Reed et al. 2016), confirming Schaffenroth et al. (2014).

Having spin rates measured from both p and gmodes provide a test of rotation as a function of radius. On the basis of a tentative measurement from a single p-mode multiplet, PHL 457 appears to

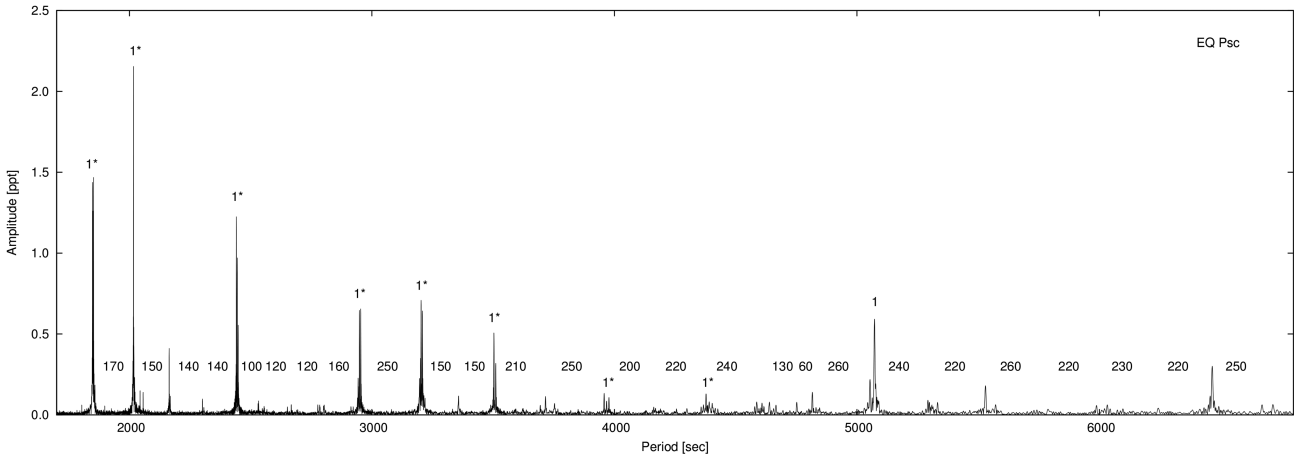

Figure 17. The amplitude spectrum of EQ Psc as a function of period, instead of frequency. The numbers between peaks denote period spacing in seconds, while numbers with asterisks above peaks denote modal degrees identified from multiplets.

show differential rotation, with the envelope spinning faster than the core.

We show the intermediate-frequency region in Fig. 8. The top panel shows the entire region with significant peaks. The lower panels include close-ups of the multiplet candidates. In the second panel from the top, we detected three peaks at frequencies separated by around 2.5 μHz or multiples thereof. There are three peaks with amplitudes below the detection threshold at frequencies split by 2.5 μHz indicated by arrows (Fig. 8). Overall, this panel shows evidence for at least a few frequencies separated by 2.5 μHz, and points at a mode with $\ell \geq 3$. The second panel from the bottom shows five significant frequencies split by 2.5 μHz and indicates at least a quadrupole mode ($\ell \geq 2$). The bottom panel includes three frequencies split by 2.5 μHz, which suggests a dipole or higher mode. Although the intermediate region is not very rich, most of the detected frequencies belong to identifiable multiplets and are therefore partially constrained. Their nature, whether p or g modes, cannot immediately be identified from their frequencies. However, the splitting of 2.5 μHz, which is twice that detected among g modes, suggests that our identification of the small-period spacing among g modes is correct.

Fig. 9 shows the amplitude spectrum of the g-mode region as a function of period, instead of frequency. We marked the periods identified and the period spacings between them. For multiplets, identification is easier, since the multiplicity indicates the modal degree. Here all easily identified multiplets are triplets, implying $\ell = 1$, with a regular period spacing of ≈250 s. For periods that are not members of a multiplet, identification is based solely on the period spacing. This may cause some ambiguity for $P > 4000$ s, where our identification may not be correct. The exceptions are f_{12}, f_{13}, and f_{14}, which show a frequency splitting equivalent to other multiplets. The absence of identifiable quadrupole or higher order modes ($\ell \geq 2$) provides no supporting evidence for our identifications. Fig. 10 shows the échelle diagram for dipole modes. We estimated the average period spacing to be 259(2) s. The sequence is not long but a hook feature is clearly present. Establishing what causes these hook features, sometimes associated with the trapping of modes in specific regions of the interior and seen in many sdBV stars with asymptotic sequences (e.g. Baran & Winans 2012), will help constrain future models of sdB interiors.

5 EQ PISCIUM

EQ Psc (= PB 5450, $\alpha_{2000} = 23^{\rm h}34^{\rm m}34.63^{\rm s}$, $\delta_{2000} = -01^{\circ}19'37.0''$) was identified as a variable sdB star by Green et al. (2003) and observed during the initial 9-d engineering test of the *K2* mission (Jeffery & Ramsay 2014). That run was long enough to measure a precise orbital period and identify a number of other periods below 50 c/d, which were attributed to gravity modes. However, the short observing run excluded the detection of multiplets or period spacings necessary for mode identification. EQ Psc has been monitored with the *Gaia* satellite. Its parallax of 2.04(11) mas translates to a distance of 489(25) pc. The *Gaia G*-band brightness is 13.04 mag (Gaia Collaboration 2018).

EQ Psc was observed again during *K2* Campaign 12, which lasted around 80 d. Only these data have sufficient resolution to estimate modal degrees and spin period.

5.1 Spectroscopic results

A circular-orbit RV fit to the RV data points reported in Table 2 yields an RV amplitude of the sdB primary $K_1 = 34.9(1.6)\,{\rm km\,s^{-1}}$ (Table 6), both for a free-period fit and while keeping the period fixed to the photometric *K2* value (Section 5.2). The mass function provides a lower limit to the companion mass $M_2 > 0.11\,{\rm M_\odot}$ (assuming $M_{\rm sdB} = 0.47\,{\rm M_\odot}$) and a minimum orbital separation $3.0\,{\rm R_\odot}$. The canonical sdB mass assumption makes the companion an M dwarf (dM) star. Fitting an eccentric orbit to the RV measurements yields an eccentricity $e = 0.11(4)$, but more precise RV measurements from high-resolution spectroscopy are required to confirm an eccentric orbit.

After folding the 24 ALFOSC spectra into 10 orbital phase bins, we fitted $T_{\rm eff}$ and $\log g$ as we did for PHL 457 to obtain the results shown in Fig. 11. It is clear that the sdB $T_{\rm eff}$ is a function of orbital phase. This effect has been seen in a number of HW Vir systems and was first noted by Wood & Saffer (1999), who found an orbital face variation as high as 1500 K for HW Vir. The explanation of this effect is simply the contamination due to the additional flux from the heated side of the secondary which is veiling the Balmer lines of the primary in such a way that they appear shallower than they really are and consequently the fit gives higher temperatures.

Table 5. Frequency list of PHL 457 obtained with pre-whitening. The detection threshold equals 0.022 ppt. The n values are relative to an arbitrary zero-point n_0.

ID	Frequency (μHz)	Period (s)	S/N	$n - n_0$	l	m
$f_{\rm bin}$	36.99084(6)	27033.719(41)	1255.5			
$f_{\rm har}$	73.9848(10)	13516.29(19)	69.4			
f_1	152.4678(9)	6558.763(40)	75.8	25	1	
f_2	155.3691(36)	6436.29(15)	19.8			
f_3	157.8000(31)	6337.13(13)	22.6	24	1	
f_4	161.766(7)	6181.77(27)	10.1			
f_5	162.953(6)	6136.72(21)	12.8			
f_6	164.2147(19)	6089.59(7)	38.3	23	1	
f_7	169.6870(25)	5893.20(9)	28.3	22	1	−1
f_8	170.9575(15)	5849.41(5)	48.2	22	1	
f_9	178.2921(34)	5608.77(11)	21.0	21	1	
f_{10}	186.573(5)	5359.82(14)	14.0	20	1	
f_{11}	196.025(6)	5101.39(16)	11.8	19	1	
f_{12}	205.3155(18)	4870.553(42)	40.6	18	1	−1
f_{13}	206.55214(34)	4841.393(8)	210.6	18	1	0
f_{14}	207.774(6)	4812.92(14)	12.0	18	1	+ 1
f_{15}	217.8207(25)	4590.93(5)	28.0	17	1	
f_{16}	219.0494(24)	4565.18(5)	29.1			
f_{17}	224.283(5)	4458.66(10)	14.0			
f_{18}	226.0398(19)	4424.000(37)	37.2			
f_{19}	231.7513(12)	4314.970(22)	60.8	16	1	
f_{20}	242.400(6)	4125.41(10)	12.6			
f_{21}	247.5674(38)	4039.30(6)	18.7	15	1	−1
f_{22}	248.8015(7)	4019.268(12)	96.6	15	1	0
f_{23}	264.2792(15)	3783.877(22)	46.5	14	1	−1
f_{24}	265.52599(16)	3766.1097(23)	444.5	14	1	0
f_{25}	266.7572(12)	3748.727(17)	60.3	14	1	+ 1
f_{26}	268.0434(37)	3730.74(5)	19.3			
f_{27}	281.894(8)	3547.43(10)	8.5			
f_{28}	283.924(9)	3522.06(11)	8.1			
f_{29}	285.1718(16)	3506.659(19)	45.9	13	1	−1
f_{30}	286.4269(6)	3491.293(8)	114.0	13	1	0
f_{31}	287.6558(8)	3476.377(10)	87.1	13	1	+ 1
f_{32}	309.0883(8)	3235.321(8)	93.0	12	1	−1
f_{33}	310.34357(37)	3222.2352(39)	190.3	12	1	0
f_{34}	311.5743(8)	3209.507(8)	89.7	12	1	+ 1
f_{35}	322.498(8)	3100.80(8)	8.4			
f_{36}	335.556(9)	2980.12(8)	8.2	11	1	−1
f_{37}	336.7869(7)	2969.236(6)	108.8	11	1	0
f_{38}	338.0124(11)	2958.472(9)	66.4	11	1	+ 1
f_{39}	553.300(7)	1807.338(24)	9.5			
f_{40}	657.963(6)	1519.842(13)	12.5			
f_{41}	660.490(8)	1514.028(18)	9.1			
f_{42}	665.524(8)	1502.576(18)	8.8			
f_{43}	671.772(7)	1488.600(15)	10.4			
f_{44}	674.263(5)	1483.101(11)	14.1			
f_{45}	676.7661(23)	1477.615(5)	30.8			
f_{46}	679.652(11)	1471.340(23)	6.7			
f_{47}	681.826(9)	1466.651(19)	7.9			
f_{48}	706.408(9)	1415.612(17)	8.2			
f_{49}	717.833(10)	1393.083(19)	7.3			
f_{50}	764.374(7)	1308.260(12)	9.7			
f_{51}	766.876(6)	1303.992(10)	12.7			
f_{52}	769.3619(37)	1299.778(6)	19.0			
f_{53}	1538.729(6)	649.8870(26)	11.3			
f_{54}	2734.218(9)	365.7353(12)	7.8			
f_{55}	2778.050(8)	359.9648(10)	9.2			
f_{56}	3652.7513(47)	273.76625(36)	14.9			
f_{57}	3660.320(7)	273.2001(6)	9.5			
f_{58}	3664.799(6)	272.86627(45)	11.8			

Table 6. Results of a circular orbital fit to the RVs of EQ PSc.

γ	System velocity ($\rm km\,s^{-1}$)	25.9(1.3)
K_1	Radial velocity ($\rm km\,s^{-1}$)	34.9(1.6)
P	Orbital period (d)	0.800880 (97)
T_0	Reference epoch (BJD−2457000.0)	650.063(7)
	Rms ($\rm km\,s^{-1}$)	7.03

For EQ Psc, $T_{\rm eff}$ varies with an amplitude of 384(44) K, and much larger than the error on the measurement of $T_{\rm eff}$ in a single phase bin. The median error of all bins is ±87 K. Therefore, following Wood & Saffer (1999), we adopt the atmospheric parameters derived at orbital phases when the sdB is farthest from us and when the dM contribution to the total flux is minimum.

Using only ALFOSC spectra taken around $-0.1 < \phi < 0.1$ (red delimiters in Fig. 11), we find for the sdB in EQ Psc: $T_{\rm eff} = 28\,320(50)$ K, $\log g/(\rm cm\,s^{-2}) = 5.632(15)$, and $\log N_{\rm He}/N_{\rm H} = -2.80(6)$.

An independent fit to the MagE spectrum from the same phases gives $T_{\rm eff} = 28\,995$ K, $\log g/(\rm cm\,s^{-2}) = 5.61$, and $\log N_{\rm He}/N_{\rm H} = -2.88$. Errors are formal so too small to be representative. The fitting method and fully blanketed LTE model atmospheres were based on Jeffery, Woolf & Pollacco (2001) and Behara & Jeffery (2006).

5.2 SED and mass determination

We attempted to fit the SED of EQ Psc as we did for PHL 457, and assuming $E(B-V) = 0.034^{+0}_{-0.031}$ (Lallement et al. 2019). It is immediately clear from the fit that, unlike for PHL 457, it is not possible to fit EQ Psc with just a single component. The best-fitting solution shown in Fig. 12 indicates a $T_{\rm eff}$ for the secondary of ∼7000 K. Note that the archival optical and infrared (IR) photometry used in the SED fit are all averages of multiple measurements obtained over periods longer than the orbital period, and so effectively phase averages.

To model the contribution from the dM companion on the SED, Kurucz (1979) atmosphere models were used. We fit the SED once with $T_{\rm eff}$ of the sdB fixed to the value of the spectroscopic analysis. We also find a solution with $T_{\rm eff}$ of the sdB allowed to vary freely. The results are shown in Table 7, while the SED and best-fitting model ($T_{\rm eff}$ free) is shown in Fig. 12. Again, the reduced χ^2 is larger than 1.0, which is likely partially caused by underestimation of the photometric errors and partially by the fact that the excess caused by the companion cannot be modelled very well with a Kurucz models.

For this system, the difference between free and constrained $T_{\rm eff}$ is larger than for PHL 457. This is partly due to the extra degrees of freedom caused by inclusion of the cool companion. However, letting $T_{\rm eff}$ to vary freely does not improve the fit significantly. To derive the mass of the sdB component only the radius of the SED fit and the surface gravity of the spectroscopic fit are used. The mass found for the free $T_{\rm eff}$ is $0.28 \pm 0.10\,\rm M_\odot$, while for the constrained fit $0.38 \pm 0.05\,\rm M_\odot$ is found. Both values are consistent within their errors, but both are on the low side. The value of the constrained fit allows for a canonical sdB, while that of the free fit does not. However, since the error on the surface gravity is likely underestimated, the real error on the mass of the sdB component is also underestimated. Since the free fit does not offer significant improvement, and $T_{\rm eff}$ can be estimated more accurately from the spectroscopic fit, the mass from the constrained fit is likely to be

Table 7. Results of the SED fit for EQ Psc based on a *Gaia* distance 489 ± 25 pc and extinction $E(B-V) = 0.034^{+0}_{-0.031}$. Hot and cool components are denoted by subscripts 1 and 2 respectively. In the first fit $T_{\rm eff,\,1}$ is free. In the second, it is fixed to the spectroscopic value. The mass is determined from the radius of the SED fit and the surface gravity of the spectroscopic fit. For the spectroscopic values, the average values of those derived from the ALFOSC and MagE spectra were used.

Fit	$T_{\rm eff,\,1}$ (K)	R_1 ($R_\odot$)	L_1 ($L_\odot$)	M_1 ($M_\odot$)	$T_{\rm eff,\,2}$ (K)	R_2 ($R_\odot$)	L_2 ($L_\odot$)	Red. χ^2
Free	32500 ± 3500	0.14 ± 0.02	16.7 ± 2.5	0.28 ± 0.10	7200 ± 500	0.25 ± 0.02	0.15 ± 0.05	8
Fixed	28690 ± 340	0.16 ± 0.01	14.6 ± 1.8	0.38 ± 0.05	6800 ± 400	0.23 ± 0.02	0.11 ± 0.03	8.38

more accurate. However, a safer conclusion would be that the mass of the sdB star cannot be constrained very well by this means.

5.3 Binary orbit from *K2* data

EQ Psc is a binary system consisting of an sdB star and a cool companion. After phase folding over the orbital period, the binned light curve is shown in the top panel of Fig. 4 and again in the upper part of Fig. 13. In the latter, we added RV data to show the correlation between flux and RV. We phased the light curve with the ephemeris

$$T = 2457738.54937(16)\,\mathrm{BJD} + 0.800826(5)E.$$

derived the same way as in the case of PHL 457. We take the reference epoch to be when the sdB star is first at its farthest from us after commencement of the *K2* observations.

Similar to PHL 457, we fit the folded light curve of EQ Psc (Fig. 4) with the following function:

$$a/(\mathrm{ppt}) = 10.649(7)\cos(2\pi(\phi+0.5)) + 1.417(7)\cos(4\pi(\phi+0.5)) + 0.055(5).$$

The significant double-sinusoidal component in the flux variation confirms again that the secondary star is likely a cool star, with additional flux coming from its illuminated side. We found no signatures of eclipses down to 0.1 ppt (1 per cent of flux's amplitude). Together with $R_1 = 0.16 \pm 0.01\,R_\odot$ from the SED fit and, assuming $R_2 \approx 0.11\,R_\odot$ for an M dwarf, we limit the orbital inclination to $i < 85^\circ$ from the absence of eclipses.

We phase fold the RV curve on the same ephemeris as the light curve. The flux minimum correlates with the zero value of RV as expected for the reflection effect.

5.4 Pulsation properties

Fig. 14 shows the frequency amplitude spectrum computed from Campaign 12 of *K2* observations. It contains significant signal at very low frequencies, indicative of the orbital period and its first harmonic (second panel from top), in the g-mode region (second panel from bottom) and some signal in the so-called intermediate and p-mode regions (bottom panel). Unlike PHL 457, the profiles of the peaks in the amplitude spectrum of EQ Psc look complex, which may indicate unstable periods/amplitudes. We pre-whitened those frequencies that are easily removed and have amplitudes above the detection threshold of 0.024 ppt, defined as for PHL 457. We recovered 102 frequencies listed in Table 8 including the binary frequency and its first harmonic.[3]

The p-mode region contains few peaks; the dominant one is shown in the bottom panel of Fig. 15. Although there is local structure which may form part of a multiplet, it is inconclusive, and the splitting is not consistent with that detected among g-modes multiplets. For solid body rotation, the p-mode splitting should be twice that of $\ell = 1$ g-modes. Otherwise, splitting should be narrower or wider, depending on the envelope-to-core spin ratio.

The g-mode region includes a few tens of frequencies including a few clear multiplet candidates, four of which are plotted in the top four panels of Fig. 15. They all show a consistent $\ell = 1$ splitting of 0.615 μHz, which translates to a rotation period ≈9.4 d. Such slow rotation clearly indicates subsynchronous rotation of the sdB star. With three components, these specific multiplets are likely dipole modes, though higher degrees cannot be completely ruled out.

The top panel of Fig. 16 shows the intermediate region, which is wider than in PHL 457; the signals are of lower amplitude and spread over a wider range. At the lowest frequencies, we found a high-amplitude signal which turned out to be split (Fig. 16, second panel from top). The splitting is not consistent with that among g-modes. If this mode were a high-degree g or p mode, it would have splitting of around 1.2 μHz. The splitting we estimated is closer to 0.5 μHz. The other candidates for split modes shown in lower panels of Fig. 16 have splittings of around 0.7 or 1.4 μHz. Perhaps in some cases we only detected alternate components and therefore the actual splitting should be half that observed. The split modes detected in the intermediate region do not help mode identification. They may be rotational multiplets, but neither modal degree nor whether they are g or p modes can be established.

We made an attempt to look for equally spaced modes in periods. Fig. 17 shows an enlargement of the g-mode region plotted in period, instead of frequency. Unlike PHL 457, we do not see a clear sequence of dipole modes and hence applied a *Kolmogorov–Smirnov* (K-S) test. This test is useful to identify a period spacing, if one exists. Using the list from Tables 5 and 8, we applied the test to both EQ Psc and PHL 457. Fig. 18 shows the K-S statistic Q which is the probability that spacings are randomly distributed. A given spacing is significant at a 'confidence level' of $(1-Q)\times 100$ per cent. To avoid biasing the test with low radial-order modes far from the asymptotic limit, we only considered periods >2900 s. For PHL 457, the common 260 s period spacing is clearly recovered with confidence > 99.999 per cent. The spacing at 130 s is simply half the 260 s spacing. Common spacings of ≈260 and ≈155 s are evident at the 99.5 per cent and 99.9 per cent confidence levels in EQ Psc. This is a marginal detection, even though the detection of a similar number of frequencies was sufficient to find a common spacing in other sdBV stars observed during the *K2* mission.

[3]From the short engineering run of *K2* in 2014, Jeffery & Ramsay (2014) reported the binary frequency and its first harmonic along with 16 other frequencies. We confirm 14 of those frequencies with substantially improved precision. Two frequencies found by Jeffery & Ramsay (2014), $f_{\rm L+}$ and $f_{\rm L-}$, are not present in our analysis and are likely related to the first multiple of the thruster firings artefact.

Table 8. Frequency list of EQ Psc obtained with pre-whitening. The detection threshold equals 0.024 ppt.

ID	Frequency (μHz)	Period (s)	S/N	*l*	*m*
$f_{\rm bin}$	14.45268(10)	69191.34(46)	1794.7		
$f_{\rm har}$	28.90535	34595.67	238.7		
f_1	104.4587(29)	9573.16(26)	24.2		
f_2	148.895(5)	6716.16(24)	13.0		
f_3	149.9228(45)	6670.10(20)	15.4		
f_4	154.6760(11)	6465.125(46)	62.7		
f_5	165.769(6)	6032.48(21)	12.3		
f_6	167.006(6)	5987.82(23)	10.8		
f_7	180.8252(18)	5530.20(6)	38.0		
f_8	187.5265(46)	5332.58(13)	15.3		
f_9	188.9320(33)	5292.91(9)	21.3		
f_{10}	197.1419(5)	5072.489(14)	126.5	1	–
f_{11}	207.6317(24)	4816.22(5)	29.5		
f_{12}	210.4433(43)	4751.87(10)	16.0		
f_{13}	214.303(6)	4666.28(14)	11.2		
f_{14}	215.5570(43)	4639.14(9)	16.1		
f_{15}	216.9909(41)	4608.49(9)	16.9		
f_{16}	218.0010(41)	4587.13(9)	16.8		
f_{17}	232.639(9)	4298.51(17)	7.5		
f_{18}	234.963(9)	4255.99(16)	8.0		
f_{19}	251.4059(36)	3977.63(6)	19.6		
f_{20}	252.0320(47)	3967.75(7)	15.2		
f_{21}	252.6772(27)	3957.618(42)	26.4		
f_{22}	266.4357(49)	3753.25(7)	14.3		
f_{23}	269.1202(31)	3715.811(42)	22.7		
f_{24}	270.713(7)	3693.94(9)	10.4		
f_{25}	284.8487(12)	3510.636(14)	60.2	1	−1
f_{26}	285.4511(7)	3503.227(8)	102.0	1	0
f_{27}	297.8545(26)	3357.344(29)	27.1		
f_{28}	311.7162(6)	3208.046(6)	130.3	1	−1
f_{29}	312.2119(5)	3202.953(6)	140.1	1	0
f_{30}	312.5008(17)	3199.992(17)	45.1	1	+ 1
f_{31}	338.5256(6)	2953.9864(49)	125.7	1	−1
f_{32}	339.1362(6)	2948.668(5)	119.4	1	0
f_{33}	339.7466(16)	2943.370(14)	42.6	1	+ 1
f_{34}	343.184(7)	2913.89(6)	10.6		
f_{35}	356.732(6)	2803.227(45)	12.2		
f_{36}	359.108(6)	2784.679(46)	11.9		
f_{37}	360.0980(50)	2777.022(38)	14.1		
f_{38}	374.911(6)	2667.298(42)	11.8		
f_{39}	377.170(6)	2651.327(45)	10.9		
f_{40}	391.334(7)	2555.359(46)	9.8		
f_{41}	394.846(6)	2532.635(37)	13.3		
f_{42}	395.186(9)	2530.45(6)	8.9		
f_{43}	408.4043(7)	2448.5543(42)	101.0	1	−1
f_{44}	409.02168(41)	2444.8582(25)	172.8	1	0
f_{45}	409.63074(29)	2441.2231(17)	242.5	1	+ 1
f_{46}	433.477(6)	2306.927(30)	12.3		
f_{47}	434.5229(35)	2301.375(18)	20.1		
f_{48}	461.1154(27)	2168.655(13)	26.2	1	−1
f_{49}	462.1356(8)	2163.8670(38)	86.5	1	0
f_{50}	486.2609(25)	2056.509(11)	27.6		
f_{51}	489.2459(25)	2043.962(11)	27.4		
f_{52}	495.0887(12)	2019.8399(49)	58.2	1	−1
f_{53}	495.75530(15)	2017.1242(6)	460.6	1	0
f_{54}	496.3930(12)	2014.5327(47)	60.5	1	+ 1
f_{55}	526.724(8)	1898.529(27)	9.2		
f_{56}	538.1700(18)	1858.149(6)	38.1		
f_{57}	539.93725(21)	1852.0671(7)	340.9	1	−1
f_{58}	540.56497(22)	1849.9164(8)	326.9	1	0
f_{59}	541.18555(22)	1847.7951(8)	319.9	1	+ 1
f_{60}	554.397(7)	1803.760(22)	10.5		

Table 8 – *continued*

ID	Frequency (μHz)	Period (s)	S/N	*l*	*m*
f_{61}	679.959(10)	1470.677(21)	7.1		
f_{62}	686.305(12)	1457.077(25)	6.0		
f_{63}	851.6539(23)	1174.1859(32)	31.1		
f_{64}	852.1252(13)	1173.5364(18)	55.9		
f_{65}	852.7734(26)	1172.6445(36)	27.9		
f_{66}	853.1149(21)	1172.1750(29)	34.3		
f_{67}	950.200(14)	1052.411(15)	5.0		
f_{68}	1079.874(12)	926.034(10)	6.1		
f_{69}	1080.509(8)	925.489(7)	9.2		
f_{70}	1081.110(16)	924.976(14)	4.4		
f_{71}	1081.752(9)	924.427(8)	8.0		
f_{72}	1082.375(12)	923.895(10)	5.8		
f_{73}	1097.907(16)	910.824(13)	4.4		
f_{74}	1149.252(12)	870.132(9)	6.0		
f_{75}	1153.054(8)	867.262(6)	8.2		
f_{76}	1154.375(12)	866.270(9)	5.7		
f_{77}	1159.430(9)	862.493(7)	7.7		
f_{78}	1471.043(15)	679.790(7)	4.6		
f_{79}	1472.253(9)	679.2310(41)	7.8		
f_{80}	1482.980(14)	674.318(6)	4.9		
f_{81}	1552.413(12)	644.158(5)	5.7		
f_{82}	1553.824(11)	643.5736(44)	6.5		
f_{83}	1599.857(11)	625.0559(42)	6.5		
f_{84}	1605.290(7)	622.9403(27)	10.1		
f_{85}	1613.656(13)	619.711(5)	5.2		
f_{86}	1720.689(13)	581.1626(45)	5.2		
f_{87}	1722.027(9)	580.7111(29)	8.2		
f_{88}	1790.605(9)	558.4705(28)	7.8		
f_{89}	1791.305(9)	558.2522(29)	7.6		
f_{90}	1795.468(17)	556.958(5)	4.0		
f_{91}	1964.732(13)	508.9754(33)	5.5		
f_{92}	2142.595(13)	466.7239(29)	5.2		
f_{93}	2247.167(10)	445.0047(19)	7.2		
f_{94}	2278.357(14)	438.9127(28)	4.9		
f_{95}	2290.482(13)	436.5893(25)	5.3		
f_{96}	4961.135(8)	201.56678(34)	8.3		
f_{97}	4962.5530(39)	201.50918(16)	17.7		
f_{98}	4966.052(13)	201.3672(5)	5.5		
f_{99}	4969.025(12)	201.24674(49)	5.8		
f_{100}	5434.703(14)	184.00269(49)	4.8		
f_{101}	5623.667(11)	177.81992(35)	6.3		
f_{102}	6947.688(6)	143.93277(12)	11.9		

We note that the SED-fit estimates of the radius of the secondary component are lower limits, since it is not clear how much of the projected stellar disc of the secondary is contributing to the observed excess. This contribution depends on the orbital inclination, and on the phases at which the photometric SED data were obtained. Taking the results for M_1, R_2, and L_2 from Table 7 for fixed $T_{\rm eff}$ at face value, while comparing the R_2, and L_2 values with those of masses for typical lower part of the main-sequence stars of 0.11–0.15 $M_\odot$, and using the spectroscopic mass-function constraints, we find that the orbital inclination must have an intermediate value of 40°–60°.

6 DISCUSSION AND SUMMARY

We have presented new photometric and spectroscopic observations of PHL 457 and EQ Psc, two close binary systems each consisting of an sdB star with a cool companion. For EQ Psc, we present the first spectroscopic orbital solution, while for PHL 457 we confirm the orbital solution presented earlier by Schaffenroth et al. (2014).

Table 9. sdB stars with orbital and rotation periods estimated. The 'method' column includes the features that were used to estimate the rotation periods.

Star	P_{orb} (d)	P_{rot} (d)	Companion	Method
		Core rotation		
PHL 457[1]	0.3	18	dM	g modes
KIC 11179657[2]	0.39	7.26	dM	g modes
KIC 2438324[2]	0.4	9.5	dM	g modes
KIC 2991403[2]	0.44	10.5	dM	g modes
EQ Psc[1]	0.8	38	dM	g modes
PG 1142-037[3]	0.5	>45	WD	g modes
KIC 7664467[4]	1.56	35	WD	g modes
EPIC 211696659[5]	3.2	>28	WD	g modes
KIC 10553698[6]	3.4	41	WD	g modes
KIC 11558725[7]	10	44	WD	g modes
KIC 7668647[8]	14.2	47	WD	g modes
		Surface rotation (per cent)		
CD−30° 11223[9]	0.049	$0.089 \pm 10 \sin i$	WD	Spectral lines
PG 1621 + 476[10]	0.070	$0.195 \pm 10 \sin i$	dM	Spectral lines
NY Vir[11]	0.101	0.101 ± 10	dM	Spectral lines
HW Vir[12]	0.115	0.115 ± 10	dM	Spectral lines
2M 1938 + 4603[12]	0.126	0.126 ± 10	dM	Spectral lines
AA Dor[13]	0.261	0.261 ± 10	dM	Spectral lines

Notes: 1: this paper, 2: Baran & Winans (2012), 3: Reed et al. (2016), 4: Baran et al. (2016), 5: Reed et al. (2018b), 6: Østensen et al. (2014), 7: Telting et al. (2012), 8: Telting et al. (2014), 9: Vennes et al. (2012), 10: Schaffenroth et al. (2014), 11: Vučković et al. (2009), 12: unpublished, and 13: Vučković et al. (2016).

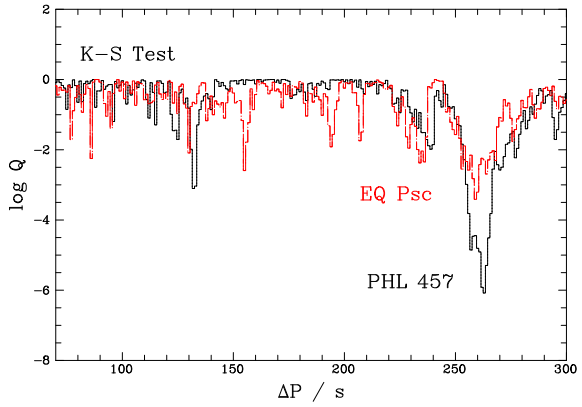

Figure 18. *K-S* test to identify regular spacings (ΔP) in sequences of periods with the same modal degree for PHL 457 (solid black) and EQ Psc (broken red) using data from Tables 5 and 8 with periods >2900 s.

For both objects, the light curves show variations caused by stellar oscillations and the reflection effect. By the latter, we mean the additional flux coming from the cool secondary which is due to reprocessing of the harder and mostly UV radiation incident on the hemisphere facing the hot subdwarf. For a recent discussion of this process, how it affects the heated surface and how it may be modelled, see Horvat et al. (2019).

The spectroscopic data also allow us to determine T_{eff}, $\log g$, and helium abundance of the sdB stars in both binaries as a function of orbital phase (ϕ). For the sdB in EQ Psc, there is a strong T_{eff}–ϕ correlation which we ascribe to veiling of Balmer lines by the contribution of reflected light from the secondary. This contribution increases the apparent T_{eff} if the reflected light has weaker (or no) Balmer lines than the sdB star itself.

In the case of PHL 457, we do not see such a T_{eff}–ϕ correlation, which is puzzling as the orbital separation of the components in PHL 457 is half that of EQ Psc. Even though the measured amplitude of the reflection effect of PHL 457 is half that of EQ Psc, the S/N of the spectra of PHL 457 is good enough to allow us to measure a T_{eff} –ϕ correlation at half the amplitude of that measured for EQ Psc. Schaffenroth et al. (2014) show that the amplitude of the photometric reflection effect declines, as expected, towards the blue, and argue that the low-orbital RV amplitude points either to a brown-dwarf companion with a minimum mass of 28 M_{Jup}, or to a very low value of the orbital inclination. In the latter case, the companion of PHL 457 could be similar to that of EQ Psc, namely a late type M star.

We conclude that the contribution of the secondary in PHL 457 is either too low in the Balmer-line region to allow detection of a T_{eff}–ϕ correlation, or that the contribution does not have a flat spectrum without Balmer lines. In case, the secondary's contribution around the Balmer lines would be due to actual reflection of the sdB spectrum off the surface of the secondary, we do not expect a T_{eff}–ϕ correlation. This latter case may be linked to the low orbital inclination, or else due to a peculiarity of the reflection effect off a possible brown dwarf.

Binary star systems often allow for the direct measurement of their component parameters. Eclipses are usually crucial for this purpose since they constrain the inclination of the orbit to be close to 90°. An unknown inclination leads to degeneracies, and a reliable orbit solution is not possible. Our systems show a reflection effect but no eclipses and hence we estimated that the inclinations must be <78° for PHL 457 and <85° for EQ Psc. On the other hand, the amplitude of the reflection effect is <1 per cent in both cases, which may suggest low inclination. In addition, we found all components of presumably rotational triplets, which indicate a moderate inclination of 30°–60° assuming approximate equipartition of pulsation energy amongst members of a multiplet. We are aware that the amplitude of the reflection effect also depends on the radii of components. For PHL 457 this implies, if we assume the orbital and stellar inclinations to be similar, that the secondary must be a brown dwarf. Additionally, we find from (simplistic) photometric-SED modelling of the two components in EQ Psc, and from mass-function constraints, that their stellar parameters point at the orbital inclination of 40°–60°.

From our LTE fits of the atmospheric parameters, based on our new spectroscopic data, we derived values for the surface gravity of both sdB stars. In combination with the radius constrained by the *Gaia* parallax and SED modelling, we find spectroscopic masses from the surface-gravity values. We derive $M_1 = 0.39(5)\,M_\odot$ for the sdB in PHL 457, and $M_1 = 0.38(5)\,M_\odot$ for the sdB in EQ Psc. We stress that the errors cited are propagated from measurement errors, but the systematics in the LTE fits may have even a larger influence. In fact, a possible systematic correction of $\log g / \mathrm{cm\,s^{-2}}$ less than 0.1 would be sufficient to derive a canonical mass of $M_1 = 0.47\,M_\odot$ for these two sdB stars. We urge for accurate re-calibration of the spectroscopic surface-gravity measurements.

We calculated amplitude spectra and derived orbital periods of 0.312 and 0.801 d for PHL 457 and EQ Psc, respectively. We also derived tens of frequencies of oscillation modes. PHL 457 shows at least 58 frequencies, mostly g modes with some exceptions located in the intermediate and p-mode regions. EQ Psc shows at least 102 frequencies, distributed in roughly the same way. We searched for multiplets and asymptotic period spacings, two features of an amplitude spectrum that allow estimates of spin period and modal

degree. In PHL 457, we found one possible multiplet among the p modes and probable multiplets among the g modes, while in EQ Psc we found no multiplets among p modes and several multiplets among the g modes. For PHL 457, the multiplets yield spin periods of 4.6 d (core) and 2.5 d (envelope: provisional). For EQ Psc, they yield a core spin period of 9.4 d. In PHL 457, we found mode groups separated by almost 1000 μHz, which may suggest p modes of consecutive radial order (Baran et al. 2009).

The orbital and rotation periods clearly suggest that both sdB stars are rotating subsynchronously. Other sdB binaries which convincingly show this feature include KIC 11179657, KIC 2438324, KIC 2991403 (Baran & Winans 2012), PG 1142-037 (Reed et al. 2016), KIC 7664467 (Baran et al. 2016), EPIC 211696659 (Reed et al. 2018b), KIC 10553698 (Østensen et al. 2014), KIC 11558725 (Telting et al. 2012), and KIC 7668647 (Telting et al. 2014, Table 9). The first three are systems with M dwarf companions, while the other six are systems with white dwarf companions. Our analysis added two systems of the former kind, bringing the total number of subsynchronous sdB stars with cool companions to five. Even if the p-mode multiplet in PHL 457 is correctly identified, it implies subsynchronous surface rotation.

The only sdB binaries to show asteroseismic evidence for synchronous rotation are NY Vir (Charpinet et al. 2008) and Feige 48 (Van Grootel et al. 2008). From measurements of rotationally broadened lines, the short-period sdB + dM eclipsing binary HW Vir may also be synchronized to within 10 per cent (Edelmann 2008). NY Vir and HW Vir may be an exception, since the orbital period of about 3 h implies a small orbit and the tidal forces are stronger than in wider binaries. However, assuming current convection theory, tidal forces cannot synchronize *any* sdB binary (Preece, Tout & Jeffery 2018, 2019). Moreover, it is harder to spin-up the envelope without spinning up the core, since convection is the primary vector for transporting angular momentum through the star. Nevertheless, subsynchronous binaries remain important for understanding tidal processes in sdB binaries and the common envelope ejection process which leads to their formation.

ACKNOWLEDGEMENTS

ASB gratefully acknowledges financial support from the Polish National Science Center under project nos UMO-2017/26/E/ST9/00703 and UMO-2017/25/B/ST9/02218. The Armagh Observatory and Planetarium is funded by the Northern Ireland Department for Communities. This work presents results from the European Space Agency (ESA) space mission *Gaia*. *Gaia* data are being processed by the *Gaia* Data Processing and Analysis Consortium (DPAC). Funding for the DPAC is provided by national institutions, in particular the institutions participating in the Gaia MultiLateral Agreement (MLA). The *Gaia* mission website is https://www.cosmos.esa.int/gaia. The *Gaia* archive website is https://archives.esac.esa.int/gaia. This research was made possible through the use of the AAVSO Photometric All-Sky Survey (APASS), funded by the Robert Martin Ayers Sciences Fund. This publication makes use of data products from the 2MASS, which is a joint project of the University of Massachusetts and the Infrared Processing and Analysis Centre/California Institute of Technology, funded by the National Aeronautics and Space Administration and the National Science Foundation. This publication makes use of data products from the *WISE*, which is a joint project of the University of California, Los Angeles, and the Jet Propulsion Laboratory/California Institute of Technology, funded by the National Aeronautics and Space Administration.

REFERENCES

Bachulski S., Baran A., Jeffery C., Østensen R., Reed M., Telting J., Kuutma T., 2016, Acta Astron., 66, 455
Baran A., 2012, Acta Astron., 62, 179
Baran A., Pigulski A., O'Toole S. J., 2008, MNRAS, 385, 255
Baran A., Reed M., Østensen R., Telting J., Jeffery C., 2017, A&A, 597, 95
Baran A., Telting J., Nemeth P., Østensen R., Reed M., Kiaeerad F., 2016, A&A, 585, 66
Baran A. et al., 2009, MNRAS, 392, 1092
Baran A. S., Koen C., Pokrzywka B., 2015a, MNRAS, 448, 16
Baran A. S., Telting J. H., Nemeth P., Bachulski S., Krzesinski J., 2015b, A&A, 573, 52
Baran A. S., Winans A., 2012, Acta Astron., 62, 343
Baran A. S. et al., 2012, MNRAS, 424, 2686
Behara N. T., Jeffery C. S., 2006, A&A, 451, 643
Bianchi L., Herald J., Efremova B., Girardi L., Zabot A., Marigo P., Conti A., Shiao B., 2011, Ap&SS, 335, 161
Blanchette J.-P., Chayer P., Wesemael F., Fontaine G., Fontaine M., Dupuis J., Kruk J., Green E., 2008, ApJ, 678, 1329
Camarota L., Holberg J. B., 2014, MNRAS, 438, 3111
Charpinet S., Fontaine G., Brassard P., Chayer P., Rogers F. J., Iglesias C. A., Dorman B., 1997, ApJ, 483, 123
Charpinet S., Fontaine G., Brassard P., Dorman B., 2000, ApJS, 131, 223
Charpinet S., Fontaine G., Brassard P., Dorman B., 2002, ApJS, 140, 469
Charpinet S., Van Grootel V., Reese D., Fontaine G., Green E., Brassard P., Chayer P., 2008, A&A, 489, 377
Cutri R. M. et al., 2012, Explanatory Supplement to the WISE All-Shy Data Release Products
Edelmann H., 2008, in Heber U., Jeffery C. S., Napiwotzki R., eds, ASP Conf. Ser. Vol. 392, Hot Subdwarf Stars and Related Objects. Astron. Soc. Pac., San Francisco, p. 187
Edelmann H., Heber U., Altmann M., Karl C., Lisker T., 2005, A&A, 442, 1023
Edelmann H., Heber U., Hagen H.-J., Lemke M., Dreizler S., Napiwotzki R., Engels D., 2003, A&A, 400, 939
Evans D. W. et al., 2018, A&A, 616, A4
Fontaine G., Brassard P., Charpinet S., Green E. M., Randall S. K., Van Grootel V., 2012, A&A, 539, 12
Foster H., Reed M. D., Telting J. H., Østensen R. H., Baran A. S., 2015, ApJ, 805, 94
Gaia Collaboration, 2018, A&A, 616, A10
Geier S., 2013, A&A, 549, 110
Geier S., Heber U., 2012, A&A, 543, 149
Green E. M. et al., 2003, ApJ, 583, 31
Guo J.-J., Li Y., 2018, MNRAS, 478, 3290
Handler G., 2013, Asteroseismology. Springer Science + Business Media, Dordrecht
Heber U., Reid I. N., Werner K., 2000, A&A, 363, 198
Henden A. A., Levine S., Terrell D., Welch D., 2015, American Astronomical Society, Meeting #225, 336.16
Horvat M., Conroy K. E., Jones D., Prša A., 2019, ApJS, 240, 36
Jeffery C. S., Ramsay G., 2014, MNRAS, 442, 61
Jeffery C. S., Woolf V. M., Pollacco D. L., 2001, A&A, 376, 497
Kelson D. D., 2003, PASP, 115, 688
Kelson D. D., Illingworth G. D., van Dokkum P. G., Franx M., 2000, ApJ, 531, 159
Kern J., Reed M., Baran A., Telting J., Østensen R., 2018, MNRAS, 474, 4709
Ketzer L., Reed M., Baran A., Németh P., Telting J., Østensen R., Jeffery C., 2017, MNRAS, 467, 461
Kilkenny D., Koen C., 2016, MNRAS, 457, 723
Kilkenny D., Koen C., O'Donoghue D., Stobie R. S., 1997, MNRAS, 285, 640
Kurucz R. L., 1979, ApJS, 40, 1
Lallement R., Babusiaux C., Vergely J. L., Katz D., Arenou F., Valette B., Hottier C., Capitanio L., 2019, A\&A, 625, 135

Marshall J. L. et al., 2008, in McLean I. S., Casali M. M., eds, Ground-based and Airborne Instrumentation for Astronomy II, Vol. 7014. Proceedings of the SPIE, Marseille, p. 701454
Østensen R. H., Telting J. H., Reed M. D., Baran A. S., Nemeth P., Kiaeerad F., 2014, A&A, 569, 15
Østensen R. H. et al., 2012, ApJ, 753, 17
Østensen R. H. et al., 2013, A&A, 559, A35
Preece H. P., Tout C. A., Jeffery C. S., 2018, MNRAS, 481, 715
Preece H. P., Tout C. A., Jeffery C. S., 2019, MNRAS, 485, 2889
Reed M. D. et al., 2016, MNRAS, 458, 1417
Reed M. et al., 2018a, Open Astron., 27, 157
Reed M. et al., 2018b, MNRAS, 474, 5186
Reed M. et al., 2019, MNRAS, 483, 2282
Riello M. et al., 2018, A&A, 616, A3
Schaffenroth V., Classen L., Nagel K., Geier S., Koen C., Heber U., Edelmann H., 2014, A&A, 570, 70
Skrutskie M. F. et al., 2006, AJ, 131, 1163
Telting J. H. et al., 2012, A&A, 544, 1
Telting J. H. et al., 2014, A&A, 570, 129
Uzundag M., Baran A., Østensen R., Reed M., Telting J., Quick B., 2017, A&A, 597, 95
Van Grootel V., Charpinet S., Fontaine G., Brassard P., 2008, A&A, 483, 875
Vennes S., Kawka A., O'Toole S. J., Németh P., Burton D., 2012, ApJ, 759, L25
Vos J., Vučković M., Chen X., Han Z., Boudreaux T., Barlow B. N., Østensen R., Németh P., 2019, MNRAS, 482, 4592
Vos J., Zorotovic M., Vučković M., Schreiber M. R., Østensen R., 2018, MNRAS, 477, L40
Vos J., Østensen R. H., Németh P., Green E. M., Heber U., Van Winckel H., 2013, A&A, 559, A54
Vos J., Østensen R. H., Vučković M., Van Winckel H., 2017, A&A, 605, A109
Vučković M., Østensen R., Aerts C., Telting J., Heber U., Oreiro R., 2009, A&A, 505, 239
Vučković M., Østensen R., Németh P., Bloemen S., Pápics P., 2016, A&A, 586, 146
Werner K., Deetjen J. L., Dreizler S., Nagel T., Rauch T., Schuh S. L., 2003, in Hubeny I., Mihalas D., Werner K., eds, ASP Conf. Ser. Vol. 288, Stellar Atmosphere Modeling. Astron. Soc. Pac., San Francisco, p. 31
Wood J., Saffer R., 1999, MNRAS, 305, 820

This paper has been typeset from a TEX/LATEX file prepared by the author.